INTEGRATION OF FUNCTIONAL OXIDES ONTO SILICON SUBSTRATES

by

Hanu K. Arava, B.S.

A thesis submitted to the Graduate Council of
Texas State University in partial fulfillment
of the requirements for the degree of
Master of Science
with a Major in Materials Physics
August 2014

Committee Members:

Ravi Droopad, Chair

Wim Geerts

Edwin Piner

FAIR USE AND AUTHOR'S PERMISSION STATEMENT

Fair Use

Duplication Permission

ACKNOWLEDGEMENTS

I would like to use this opportunity to thank my thesis supervisor Dr. Ravi Droopad for his support and guidance throughout these past couple of years. He encouraged an environment where I had the freedom to pursue a variety of research venues and explore different ideas with ease. My journey through graduate school would not have been possible without Dr. Wim Geerts and his enthusiasm. He is a firm advocate for students and I have been fortunate enough to have him as a graduate advisor. I would also like to express my gratitude to Dr. Edwin Piner for providing invaluable insights with both theory and analysis of experimental data.

I also owe gratitude to members of the MBE group. Postdoctoral researchers Rocio, Juan and Manuel always lent a hand when in need. The Ellipsometery data provided by Javad played a key role that set the right tone for PZT growths and analysis.

A special thanks to the brilliant post-doc Craig Swartz for his patience in tending to my questions. Experimental advice from Eric Schires was the key to many stumbling blocks during this period.

Additionally, Dr. Hui Fang was responsible for providing me the right direction to pursue a path in the field of materials science.

Not the least, the unwavering support of my mom through my educational pursuits has been detrimental in my growth as a researcher.

Ferroelectric hysteresis measurements were performed by postdoctoral researcher Sandeepan Dasgupta of Penn State within Dr. Suman Datta's group.

Funding for this work was provided by SEMATECH/SRC and Air force Research.

TABLE OF CONTENTS

Page

LIST OF FIGURES

Figure **Page**

LIST OF ABBREVIATIONS

Abbreviation	Description
STO	$SrTiO_3$
BMO	$BiMnO_3$
PZT	$PbZr_{0.53}Ti_{0.47}O_3$
Si	Silicon
LNB	$LiNbO_3$
BIT	$Bi_4Ti_3O_{12}$
MBE	Molecular Beam Epitaxy
RHEED	Reflection High Energy Electron Diffraction
CSD	Chemical Solution Deposition
PLD	Pulsed Laser Deposition
XRD	X ray Diffraction
P-E	Polarization-Electric Field
MEMS	Micro-Electro-Mechanical Systems
MPB	Morphotropic Phase Boundary
XPS	X ray Photoelectron Spectroscopy
FERROFET	Ferroelectric Field Effect Transistor
DRAM	Dynamic Random Access Memory

FeRAM	Ferroelectric Random Access Memory
TGA	Thermo-gravimetric Analysis
DTA	Differential Thermal Analysis

ABSTRACT

The purpose of this thesis is to investigate the integration of functional oxides onto silicon substrates using MBE and Spin-Coating techniques. Functionality is defined, by Materials Department of Imperial College of London, as any property in a material that is not load-bearing in nature. Examples of functionalities that are not load-bearing include magnetic, electric, electro-optic, pyroelectric and many more unique types of behavior. More-than-Moore is the primary motivation within the thesis. Unlike the standard Moore's Law predicting the doubling of semiconductor devices onto a single microchip, More-than-Moore looks into increasing functionality in a single microchip.

Original work involving epitaxial growth of BMO on STO buffered Si substrates using MBE is demonstrated. Additionally successful growths of PZT, BIT and LNB on silicon and STO buffered silicon substrates using spin-coating have also been investigated. Integration of functional oxides on Si carries with it issues arising from lattice mismatch, stoichiometry, energy enthalpies and phase impurities. Therefore, structural characterizations such as RHEED, XPS and XRD have taken precedence. Ferroelectric hysteresis data for spin-coating growths involving PZT, BIT and LNB has been included.

I. INTRODUCTION

The current work falls within the domain of More-than-Moore: this is a world wherein functionality takes precedent over size. The well known Moore's Law proposed by Gordon Moore in 1965 pertains to the scaling of semiconductors devices and their integration onto a microchip. Smaller transistors lead to more transistors packed into a given microchip area and this enables for increased computing power at lower operating voltage and therefore better performance [1] [2]. The number of devices onto a microchip has doubled every ~two years since 1960s; however scaling beyond the current 11 nm node is proving to be extremely difficult due to the degradation of the properties of Si and along with this transistor switching speed that is limited by the Boltzmann limit that sets a sub-threshold swing limit on CMOS at 60 mV/decade [3] [4] [5].

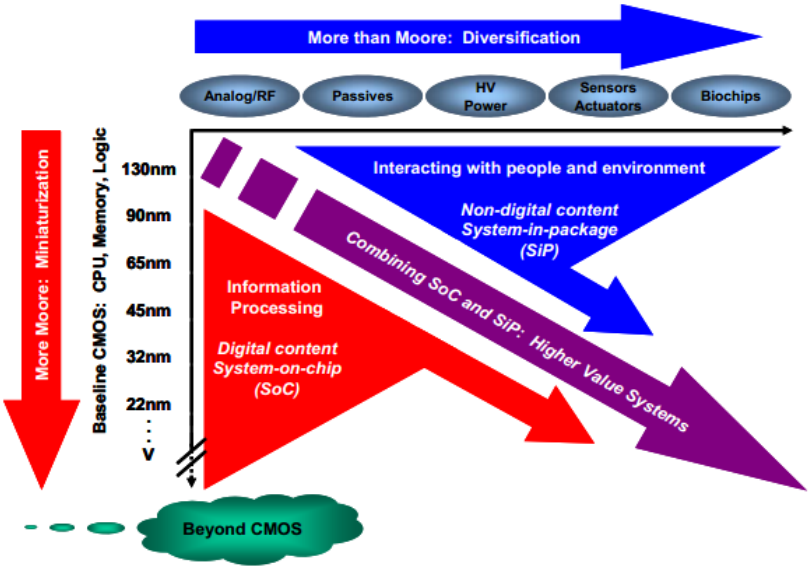

Figure 1.1: Moore's Law and More-than-Moore.

The work within this thesis is concerned with a variation of the Moore's law now labeled as More-than-Moore. As shown in the figure 1.1 taken from ITRS roadmap, More-than-Moore is about diversification. Reduced size is complemented by this increased functionality but the scaling is not on the same level as the standard Moore's law. Within this scheme, the devices are performing tasks in a wide range of fields using an array of sensors, MEMS, terahertz devices, energy applications, photovoltaics etc. This is the convergence of technologies creating a world of small yet highly functional [2].

Oxides play a major role in More-than-Moore type diversification. This work involves a class of materials that fall under the category of functional oxides. These materials are functional because they exhibit a variety of properties that render them highly useful. Examples of devices that make use of these materials range anywhere from those affecting us directly , such as personal computers, cellular phones, printers, data storage (flash drives, hard disks etc.), the world wide web, and to that of the indirect; like GPS, Supercomputers (example: weather predictions), energy storage (solar cells, electrochemical cells) etc [6] [7] [8]. Most oxides within this work belong to the perovskite family. Due to their very specific crystalline structure, they are known to exhibit both theoretically and experimentally a wide range of properties, ranging from ferroelectricity to that of ferromagnetism and even something as exotic as superconductivity [6] [7].

Perovskites carry the generic formula of ABO_3, with A and B being metal atoms. A and B sites are picked in such way that new properties are induced within a crystal for specific applications [9].

This work has its focus on oxides with the ABO_3 configuration grown on silicon substrates. Specifically, these are, STO, PZT, LNB, BIT and BMO. As far as history is concerned, no one has demonstrated a successful growth of epitaxial $SrMnO_3$ on either silicon or strontium titanate substrates. On the other hand, BMO shows a theoretical multiferroic behavior but hasn't been epitaxially grown successfully on silicon substrates although growths have been performed on STO substrates [6] [8] [10] by MBE and PLD.

In addition there is considerable interest in novel ferroelectric devices and when grown directly on semiconductors can be used in the development of non-volatile single transistor memory elements in which the ferroelectric layer is used as the gate dielectric in a MOSFET device [11]. More recently, it has been proposed that the incorporation of a ferroelectric layer as part of a gate dielectric stack can be exploited to reduce the sub-threshold swing for ultra-low power MOSFET devices [12]. Of course, the desire is to be able to integrate a single crystal ferroelectric layer on a semiconductor to achieve spontaneous polarization that is aligned along a single direction, preferably normal to the surface, as opposed to a polycrystalline or amorphous layer.

PZT is a known ferroelectric that is used in a variety of applications and thus makes for a good starting material system to investigate proof of concept designs. However lead free

materials options are a great deal of interest for environmental concerns and introduction into commercial fabrication facilities. Hence growth was performed for LNB and BIT as alternatives to PZT. As comparisons, the growths were performed both on silicon and STO/Si virtual substrates. Investigation of structural, magnetic and electrical properties along with the integration and behavior of these oxides onto silicon substrate would enable the push for real world applications by combining added functionalities with everyday electronics.

Most of the prior research for epitaxial functional oxides, in particular perovskites has been carried out using strontium titanate ($SrTiO_3$) substrates. While they make good substrate for the study of oxide growths primarily due to their close lattice match with other similar oxides, they have little to no relevance when it comes to applying technologies for the industry due to available size of the STO substrates and the increased costs with manufacturing STO substrates. In addition, large scale Si manufacturability is matured to a level that devices developed on Si substrates will require minimal investments for commercial applications. [6] [8][13].

One way to envision diversification is through the idea of nano-robots. Hypothetically these would be intelligent devices performing independent tasks in alien environments such as the insides of a human body. The requirement for such devices involves motion through MEMS, measuring vital signs through sensors, storing energy for power, memory for data collection and computing for decision making. More-than-Moore allows for such a set-up in a single device through functionalities.

For such a world to be a possibility, it is therefore imperative that work is accelerated towards integration of materials with great functionalities. The versatility of oxides [6] [8] [9] [10] makes them a perfect candidate to ensure that such a future is brought to fruition.

This research is focused primarily on the integration and partially on characterization of these fantastic materials. Their successful integration onto silicon (and III-V) and not the least their complete unraveling through a variety of characterization techniques would enable us to understand and implement these new materials into the current technologies. This would thus enable a successful maturity of More-than-Moor concept for semiconductor devices.

Given the significance of accelerating more-than-Moore within the framework of silicon integration, it thus forms for segue to introduce the background and fundamentals concerning inducing properties in oxides. The following chapter (II) is meant to be **independently recognized** as a crash course on fundamentals behind symmetry breaking and their application to determining oxide properties.

II. FUNDAMENTALS OF SYMMETRY

Introduction

Multiferroics are a class of materials showing the onset of ferroelectricity and ferromagnetism in the same phase. The term was coined by Hans Schmid in his influential 1994 paper on ferroelectrics [14]. The added flexibility to have magnetization controlled by electric field and that of polarization by a magnetic field holds options for a wide range of novel devices. There have been proposals for multiple state logic devices, sensors, RAM, high density memory storage, tunnel junctions etc [15]. Ferroelectrics and ferromagnets on their own have played a significant role hence the idea of coupling these two has generated a great deal of excitement. The history in the development of both the theory and experimental work that lead to these classes of materials is filled with some of greatest work carried out in condensed matter physics.

P.Curie in 1894 first recognized the connection between magnetic and electric properties using symmetry arguments [16]. But it wasn't until 1920; Valasek's use of Rochelle salt to demonstrate the existence of ferroelectric hysteresis that there was an increased interest in ferroic materials [17]. Symmetry considerations indicating possible antisymmetric tensors were later developed by Heesch (1929) [18] and Shubnikov (1951) [19] by the introduction of "color" symmetry. Shuvalov and Belov in 1962 extended earlier work by Heesch and Shubnikov and determined the coexistence of spontaneous polarization and magnetization in the 122 Shubnikov-Heesch point groups [20]. It is also essential to make note of the landmark 1937 work by Landau on second order phase transitions (now

known as landau's theory) giving a thermodynamic framework for both ferroelectric and ferromagnetic materials [21]. 1957 theoretical work by Landau and Lifshitz gave a simple mathematical formulation demonstrating the linear magnetoelectric effect [22]. This effect was successfully demonstrated in 1961 by Astrov [23] using Cr_2O_3 after having been theoretically predicted by Dzyaloshinskii using time-reversal symmetry arguments in 1959 [24]. Smolensky in 1958 [25] experimentally showed the existence of antiferromagnetic and ferroelectric behavior in lead perovskites:

$$Pb\left(Fe_{\frac{1}{2}}Nb_{\frac{1}{2}}\right)O_3,\ \ Pb\left(Fe_{\frac{1}{2}}Ta_{\frac{1}{2}}\right)O_3\ and\ Pb\left(Fe_{\frac{2}{3}}W_{\frac{1}{3}}\right)O_3\ .$$

Ascher in 1966 used nickel iodine boracite ($Ni_3B_7O_{13}I$) to demonstrate the simultaneous onset of ferroelectricity and weak ferromagnetism at 61 K, the first multiferroic [26].

The topic of ferroelectrics and ferromagnetism and their coupling has proved to be a stimulating task theoretically. But it wasn't until Spaldin issued an open challenge in 2000 [9] concerning the intricacies of perovskites that a significant interest has been reinstated in these special classes of materials that eventually led to viable options for devices.

We now know that perovskites are a very versatile class of materials exhibiting ferroelectricity, ferromagnetism, magnetoelectric, multiferroic, superconductive, second harmonic generation etc [8] [15]. This chapter aims to give a general overview of symmetry considerations and their challenges in applying to materials using crystalline perovskite oxides as examples whenever needed.

Crystallography Overview

Solids are divided into two unique categories based on the idea of order. Materials that possess short range order are known as amorphous whereas those with long-range fall under the category of crystalline. Amorphous materials have their own share of applications in the real world. Our interest nonetheless lies with crystalline. Long range order enables a certain degree of predictability in regards to material properties. This makes crystals a powerful class of materials. A crystal by definition has periodicity with it. Atoms or molecules form the backbone of this periodicity. Mathematically we can write this periodicity in the form of crystal symmetry. In a 3D world, there are 7 distinct crystal systems and when included the various lattice centering options that preserve the crystal symmetry we end up with 14 bravais lattices. Let us pick one point in these lattices and hold it stationary. All the possible symmetries that unfold from this action (rotations, reflections, inversions and improper rotations) form a point group. Stationary points can be more than one. Following this, we have 32 distinct point groups. Extending this further to include glide and screw translational operations, we end up with 230 space groups. The treatment of the chapter will skip space groups. This is because the translations resulting in space groups occur in the atomic scale and their influence is not prominent for macroscopic properties. Point groups on the other hand make a reliable setting for the deciphering of physical effects. Please do bear in mind that all these groups are related to position and transformations associated with it. There are properties that

have an axial component to them that look into changing the parity (odd function). An example would be magnetism (remember the right hand thumb rule!).

Electric orders

Overview

We first set out the most important rule in crystallography. This is the Neumann's rule and it states the following:

"The symmetry of any physical property of a crystal must include symmetry elements of the point group of the crystal"

Any physical property that we define for a point group will always be observed in the macroscopic material. The opposite is not necessarily true. In other words, any property that we define henceforth is therefore macroscopically acceptable as long as point groups observe them. All point groups are addressed using Hermann-Mauguin notation [27].

We will start off with the idea of inversion symmetry. This is defined using the operator (which forms a point group by itself) $\bar{1}$. Matrix notation of this follows as:

$$\begin{pmatrix} -1 & 0 & 0 \\ 0 & -1 & 0 \\ 0 & 0 & -1 \end{pmatrix}$$

Any point group that remains invariant under this transformation is considered a centrosymmetric point group. When applying this transformation to all the 32 point groups [14] [15] [9], we end up with 11 that have an inversion center. These are:

$$\bar{1}, \frac{2}{m}, mmm, \frac{4}{m}, \frac{4}{mmm}, \bar{3}, \bar{3}m, \frac{6}{m}, \frac{6}{mmm}, m3 \; and \; m3m.$$

Those with an inversion center will not have a net dipole moment and therefore can be excluded in our discussion of various electric orders. The remaining groups are non-centrosymmetric [14] [15] [9] and these are:

$$1,2,3,4,6, m, mm2,3m, 4mm, 6mm, 422,222,622,32,23$$

$$, \bar{4}2m, \bar{4}, \bar{6}, \bar{4}3m, \bar{6}2m \; and \; 432$$

Figure 2.1 shows the overall classification of all the 21 non-centrosymmetric point groups.

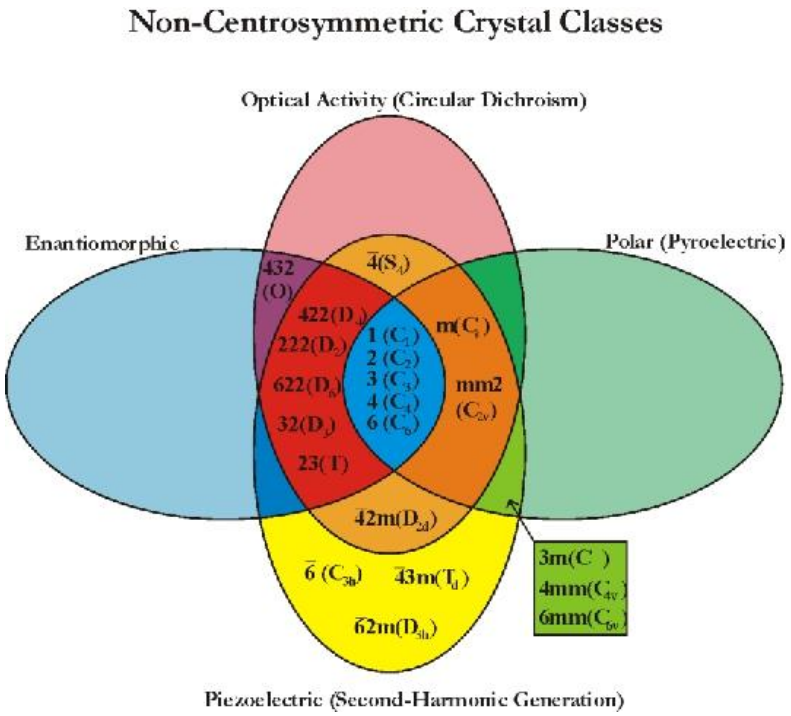

Figure 2.1: Non-centrosymmetric crystal classes [28]

Piezoelectricity

Of the 21 point groups listed only 20 are considered piezoelectric. The point group 432 is self destructive by eliminating polar behavior due to two opposing <111> axes [27]. Therefore is not included as a piezoelectric material.

Piezoelectricity is defined in two forms: These are direct and converse piezoelectric effects. Direct piezoelectric effect is the observation of polarization under stress. In the case of converse piezoelectric effect, this is the production of mechanical strain under an applied electric field. Both of these maybe written in tensor notation following Einstein summation convention as the following:

$$\text{Direct piezoelectric effect: } P_i = d_{ijk}\sigma_{jk}$$

$$\text{Converse piezoelectric effect: } \varepsilon_{ij} = d_{ijk}E_k$$

The terms involved are polarization (P_i), piezoelectric coefficient tensor (d_{ijk}), stress tensor (σ_{jk}), strain tensor (ε_{ij}) and electric field (E_k)

Examples of piezoelectricity include quartz with point group symmetry 32 [29].

This forms a perfect juncture to define a polar vector since it forms the basis for the next three electric orders. Polar vectors are physical properties that act in a preferred orientation. Electric polarization for example is a polar vector. Applying Neumann's principle [27], we can define the general transformation as:

$$T'_{ijk\ldots} = a_{il}a_{jm}a_{kn}\ldots.T_{lmn\ldots}$$

Here $a_{il}a_{jm}a_{kn}$ are the direction cosines. This operation preserves parity.

Pyroelectricity

Not all piezoelectric crystal point groups have a unique polar axis. This is the orientation in which the polar vector propagates giving rise to spontaneous polarization. Spontaneous polarization is defined as the existence of electric polarization in the absence of an electric field. Pyroelectricity is the manifestation of spontaneous polarization under temperature change. Out of the 20 piezoelectric crystals, only 10 have unique polar axis. These groups are [27]:

$$1,2,3,4,6,m,mm2,3m,4mm\ and\ 6mm$$

Therefore it can be said that Polarization (P) = Electric displacement (D). We can now lay down the mathematical foundations using pyroelectric coefficients (p) and temperature (T) as:

$$P_i = D_i$$

$$P_i = p_i \delta T$$

Applying polar transformation:

$$\delta P_i^{'} = a_{ij}\delta P_j = a_{ij}p_j\delta T'$$

$$p_i^{'} = a_{ij}p_j$$

Inversion acts on a given pyroelectric tensor using $\bar{1}$ (inversion operation):

$$\begin{pmatrix} p_1' \\ p_2' \\ p_3' \end{pmatrix} = \begin{pmatrix} -1 & 0 & 0 \\ 0 & -1 & 0 \\ 0 & 0 & -1 \end{pmatrix} \begin{pmatrix} p_1 \\ p_2 \\ p_3 \end{pmatrix}$$

This ends up giving us $p_1' = -p_1;\ p_2' = -p_2;\ p_3' = -p_3$. It is only possible if $p_1 = p_2 = p_3 = 0$. Hence materials with inversion center do not possess pyroelectricity.

An example for a pyroelectric material would be lithium tantalate ($LiTaO_3$) with point group 3m [30].

Ferroelectricity

Ferroelectrics are defined as pyroelectric materials in which we can switch the polarization by applying an electric field. This effect is hysteretic with a double well potential. All ferroelectrics are therefore pyroelectric and piezoelectric. The converse is not true. The point groups allowing ferroelectricity are [14]:

$$1,2,3,4,6,m,mm2,3m,4mm\ and\ 6mm.$$

Ferroelectricity is closely related to phase transition from a high symmetry high temperature paraelectric phase to that of a low symmetry low temperature ferroelectric phase. The theoretical background for such transition is demonstrated using landau theory in section VI.

The most standard example also happens to be the first ferroelectric oxide $BaTiO_3$. It takes ferroelectric 4mm point group symmetry at the phase transition temperature of ~400 K [31].

Magnetic Point Groups

Until now all the point groups have been concerned with polar vectors. But properties like magnetism rely on axial vectors. We can observe this in the magnetic moment vs. current relation using m for magnetic moment, i for current and A for area: $|m| = iA$.

Applying Neumann's principle yields a more generic transformation for parity operations of the form: $T'_{ijk\ldots} = |a_{il}|a_{jm}a_{kn}\ldots.T_{lmn\ldots}$ [16] with the determinant of a_{il} switching from -1 to +1 depending on parity breaking. The magnetic moment equation set out earlier resembles this odd function form by transforming as:

$$X(-t) = -X(t)$$

Visualization can be done using the changing spin of an electron. Pictorially this can be observed in figure 2.2 wherein the changing current induces a magnetic moment along axial plane.

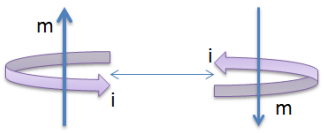

Figure 2.2: Odd transformation for magnetic moment (m) when the direction of current (i) is reversed.

This is also known as the parity operation or T-symmetry. Applying this to crystal symmetry has been a simple and elegant way of determining magnetic orders in crystals. Shubnikov and Heesch did the very same by extending the 32 point groups to involve time inversion and produced 90 additional groups called as the magnetic point groups [19] [18]. Their variation included the use of color symmetry with white and black point groups. These magnetic point groups combined with the 32 spatial groups now make up the 122 Shubnikov-Heesch point groups.

Thermodynamics

The clear way to represent thermodynamics effects on magnetic and electric properties in crystals has been by extending the Gibbs free energy in tensor notation to include electric, mechanical and magnetic work. This can be written as:

$$G = U - TS - \sigma_{ij}\varepsilon_{ij} - E_k P_k - H_i M_i \quad [32]$$

The terms used are the standard internal energy U, the temperature T and entropy S. The additional effects included are that of deformation components that include stress and strain tensors (σ & ε) , electric work using electric field (E) and polarization (P) and lastly magnetic work is represented using magnetization (M) and field strength (H).

We can also express the individual components of the extended Gibbs free energy equation by taking advantage of the partial derivatives for stress, polarization and magnetization tensors.

For example, the strain tensor may be expanded as the summation of partial derivatives using stress tensor, electric field, magnetization and temperature:

$$d\varepsilon_{ij} = \left(\frac{\partial \varepsilon_i}{\partial \sigma_{kl}}\right) d\sigma_{kl} + \left(\frac{\partial \varepsilon_i}{\partial E_k}\right) dE_k + \left(\frac{\partial \varepsilon_i}{\partial H_i}\right) dH_i + \left(\frac{\partial \varepsilon_i}{\partial T}\right) dT$$

Using this derivation in the extended Gibbs free energy relation we can obtain free energy relations for all the individual components. Continuing the focus on strain effect and expressing it in terms of the free energy, we obtain:

$\frac{\partial G}{\partial \sigma_{ij}} = -\varepsilon_{ij}$ ----> The roots of this are resolved through the partial derivatives for the extended Gibbs free energy and then having the individual differentials separated [32].

Stress and strain relations were used to define the direct and converse polarization effects. The relation between these two tensors can be obtained by defining a stiffness tensor (s) which is of the fourth rank. This relation would look like: $-\left(\frac{\partial^2 G}{\partial \sigma_{kl} \partial_{ij}}\right) = \frac{\partial \varepsilon_{ij}}{\partial \sigma_{kl}} = s_{ijkl}$. We can write down the standard strain tensor as a more encompassing effect by applying tensor transformation rules and the right coefficients as:

$$\varepsilon_{ij} = s_{ijkl}\sigma_{kl} + d_{kij}E_k + q_{lij}H_l + \alpha_{ij}\Delta T$$

This equation shows the regular stress strain relation but also strain induced effects associated with electric field, magnetic field and temperature. Similarly equations can be derived for the transformation relations concerning polarization and magnetization. Nye has an excellent discussion on this [27].

Phase Transitions

Earlier section briefly derived effects for thermodynamic relations but however these cannot be used to explain phase transitions. Conventional phase transition is imagined using the "order parameter" temperature but there can be phase transitions that are due to electric field, magnetic field, pressure etc. Developed by Lev Landau, the theory of phase transitions [21] has proven to be an excellent way to look at ferroelectric and ferromagnetic materials. Landau views phase change as a symmetry transformation and is not concerned with any microscopic effect such as atomic interactions. This makes the theory a very simple way of looking at phase transitions but is also extremely powerful.

There are two distinct orders that can be associated with phase transitions. The first order is the discontinuous type where we have the thermodynamic quantities (entropy...) observing a discontinuity. On the other hand second order shows continuity. Ferroelectric and ferromagnetic materials observe the second order phase transitions.

The theory states that in the vicinity of a phase transition we can expand the free energy using a given order parameter (we now call this the landau free energy) ,with the order parameter increasing continuously as we reach the critical temperature, using power series since the change in free energy is small enough. Both the first and second orders are demonstrated by this expansion. Ferroelectricity is set up using free energy F, the order parameter polarization (P) and electric field (E) [33]:

$$F = \frac{\alpha}{2}P^2 + \frac{\gamma}{4}P^4 + \frac{\delta}{6}P^6 - E_0P$$

Applying the Curie-Weiss law ($by\ using\ \alpha = \beta(T - T_0)$) for paraelectric to ferroelectric transition to the landau free energy with the conditions for spontaneous polarization ($E_0 = 0$), $\gamma > 0$ (condition for all second order phase transitions) and the critical temperature $(T < T_0)$, we obtain the classic double well potential (F vs. P) in figure 2.3 :

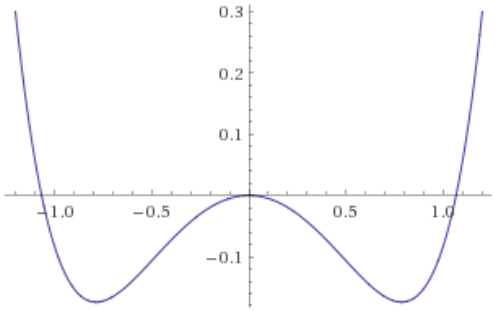

Figure 2.3: Ferroelectric double well, plotted free energy against polarization

This double well provides two stable states and also forms the source for the hysteresis curve. This is because; as much as polarization is considered spontaneous there is involvement of domain wall formation and movement. Dawber research group [34] illustrates these two stable states and the hysteretic behavior succinctly using $BaTiO_3$ as an example in figure 2.4.

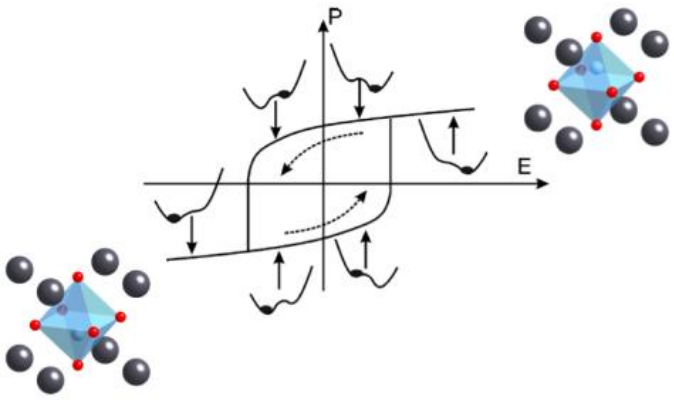

Fig 2.4: The shift in central titanium atom and the corresponding double well behavior through the hysteresis.

Magnetoelectric and Multiferroic effects

The primary interest has always been in the coupling of electric and magnetic orders. Symmetry conditions make this coupling quite easy to look at. Shuvalov and Belov derived that out of the 122 Shubnikov-Heesch point groups there are 31 point groups [20] [14] that possess spontaneous polarization and there are equal number of point groups showing spontaneous magnetization. Since we are concerned with the coexistence of spontaneous polarization and spontaneous magnetization, there are only 13 point groups [14] [9] that allow for both to exist in the same phase. These are:

$$1,2,2',m,m',3,3m',4,4m'm',m'm2',m'm',6\ and\ 6m'm'$$

This more general magnetoelectric effect can be expressed using the free energy as [15] [35]:

$$F(E,H)$$

$$= F_0 - P_i^s E_i - M_i^s H_i - \frac{1}{2}\epsilon_0 \epsilon_{ij} E_i E_j - \frac{1}{2}\mu_0 \mu_{ij} H_i H_j - \alpha_{ij} E_i H_j$$

$$- \frac{1}{2}\beta_{ijk} E_i H_j H_k - \frac{1}{2}\gamma_{ijk} H_i E_j E_k - \cdots$$

The second two terms, in the above equation, involve the spontaneous polarization and magnetization associated with ferroelectric and ferromagnetic materials. The higher order terms give us the magnetoelectric coupling factors. A clearer way of defining this can be done using the free energy derivatives with respect to electric and magnetic fields giving rise to polarization and magnetization. These are [15] [35]:

$$M_i(E,H) = -\frac{\partial F}{\partial H_i} = M_i^s + \mu_0 \mu_{ij} H_j + \alpha_{ij} E_i + \beta_{ijk} E_i H_j + \frac{1}{2}\gamma_{ijk} E_j E_k \ldots$$

The linear magnetoelectric effect can be deduced from the above equation to be:

$$P_i = \alpha_{ij} H_j \text{ and } M_i = \alpha_{ij} E_i.$$

As we can see, theoretical formulation exists for the coupling of magnetic and electric hysteretic effects. The question that needs to be looked into is how we induce these into materials.

There are certain factors that need to be part of our approach. These conditions are:

1. We need to fulfill symmetry conditions

2. Find a way to induce a double well potential for ferroelectric behavior

3. Create a pathway to support exchange mechanism that enables magnetic order.

Condition 1 is tricky. For example, all the perovskites that we have been giving accolades to until now belong to the centrosymmetric groups. By the earlier definition, a centrosymmetric point group cannot express any ferroic order. However it is know that perovskites possess these orders. The trick is in picking the right combination. In the case of $BaTiO_3$ and other titanates ($SrTiO_3$, $CaTiO_3$ etc.), the tetrahedral titanium oxide (TiO_4) is distorted and observes a ferroelectric phase transition. This transformation is from a centrosymmetric m3m to that of the non-centrosymmetric 4mm at a transition temperature of 270 K< T <400 K by having the titanium shift towards the face centered oxygen ions due to d orbital bonding with the p orbital of oxygen [31]. The distortion by the titanium shift is also termed as the second order Jahn-Teller effect [9] and is common with octahedral complexes. In the case of $SrTiO_3$ strain is the order parameter for the ferroelectric phase transition. [36]

The second condition is related to phase transitions. Without a double -well we cannot have ferroelectricity. There needs to be two stable states in a given transition state. We can use the $BaTiO_3$ as our example again. The shift in titanium holds a double well as it moves up and down passing through the center. This is the double well and is clearly observed in figure 2.4.

The third condition has more to do with chemistry than symmetry. This involves a mechanism to induce some form of exchange (double exchange, superexchange, antisymmetric exchange etc.) to encourage a magnetic order. In case of the perovskite $BiMnO_3$, Mn^{3+}-O-Mn^{3+} superexchange leads to an antiferromagnetic order [37]. Mixed perovskites such as $LaSrMnO_3$ carry multiple valence states for Mn leading to a double exchange Mn^{3+}-O-Mn^{4+} ferromagnetic order [10].

These three factors, inspired by the work of Hans Schmid [14][38], Manfred Fiebig [15] and Nicola Spaldin [9], are essential to approaching material properties in structures of perovskites and beyond.

Concluding Remarks

Symmetry is a very powerful tool to have while trying to either figure out material properties or to define new structures. Coupling of electric and magnetic ferroic orders has been achieved but is far from device realization. Symmetry arguments enable us to venture out and propose new materials with focused purposes. There is a multitude of other effects not discussed but have stared right at us during this discussion. These include Ferrotoroidic (E X H) and Ferroelastic (hysteretic mechanical deformation) effects. Higher order effects also hold very interesting prospects. These are hysteretic effects involving 2nd, 3rd ... rank tensors such as Ferrobielectric and Ferromagnetoelectroelastic [38] [15] [14]. Optical orders haven't been looked at, nonetheless they form part of the core component in perovskite properties. A successful integration of these versatile materials onto current technologies and the design of novel applications is thus a high priority assignment to advance more-than-Moore.

III. EXPERIMENTAL TECHNIQUES

Molecular Beam Epitaxy

Molecular Beam Epitaxy is an ultrahigh vacuum evaporation technique that is used to deposit high quality thin films. The typical base pressure in an MBE chamber is $<10^{-10}$ torr achieved using a combination of pumps depending on the type of materials grown in the system. For example, ion pumps and cryopumps are used as the primary pumps in a solid source compound semiconductor chamber. On the other hand, an oxide MBE chamber would have a combination of turbomolecular and cryopumping; the use of the turbomolecular pump is necessitated for the need to pump oxygen during growth. The low base pressure allows for the growth of crystals having little to no impurities thereby allowing for the study of the basic properties of a particular material system. Because MBE is a non-equilibrium growth technique, it is possible to deposit metastable structures and design properties using bandgap engineering to tailor specific applications.

The oxide MBE chamber used in this study contains elemental sources and uses molecular oxygen during the growth. The figure below (figure 3.1) is a typical MBE chamber used during the course of this research. Each source is contained in an effusion cell which is heated to generate a flux of the source material needed for the deposition of the relevant compound. The growth rates used during oxide growth are extremely slow and are usually on the order of 4 Å/min, limited by the temperature at which the Ti cell can safely be operated to increase the lifetime. In the case of an oxide MBE, we have an additional source of oxygen and the growths are carried out at a higher pressure of $>10^{-8}$

torr .

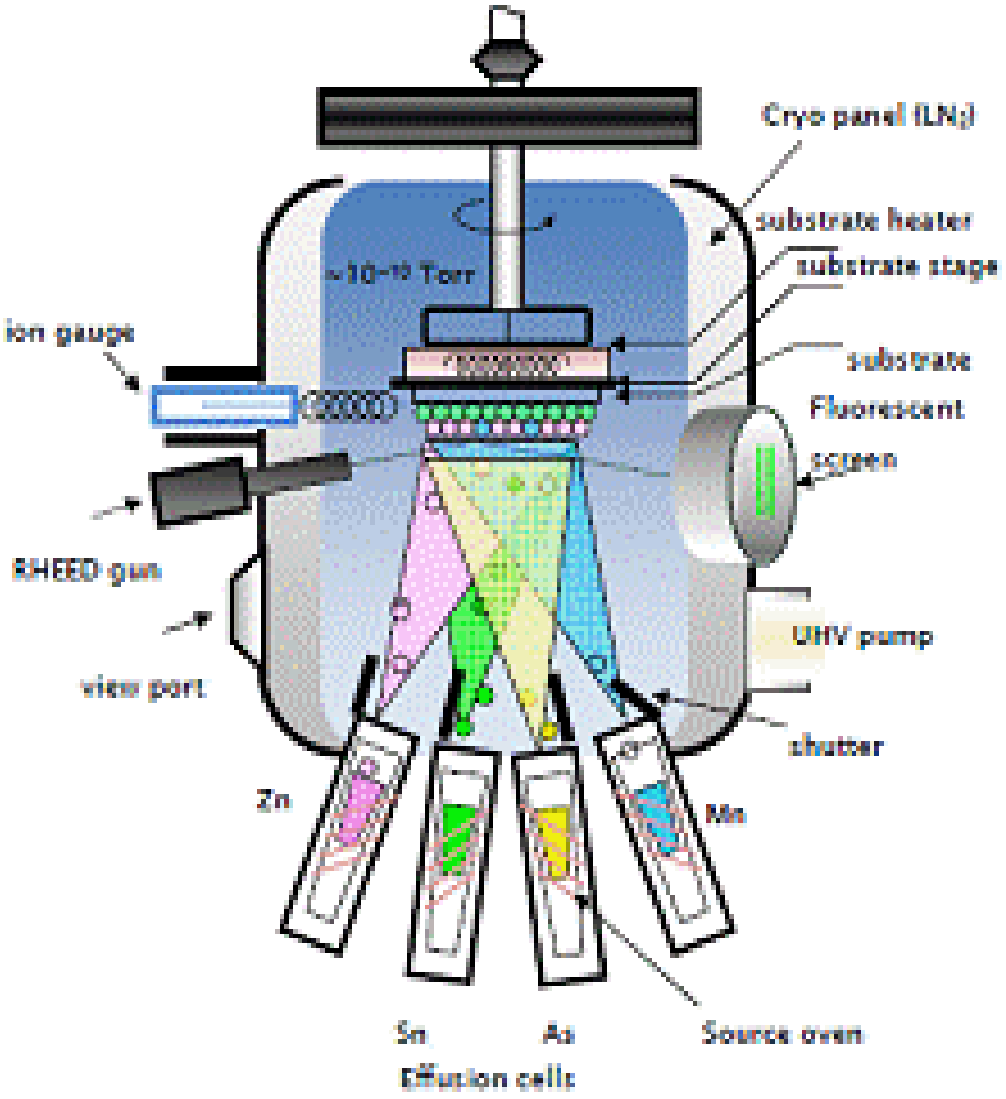

Source : http://etigo.nagaokaut.ac.jp/koudoka/sptm/Joel.htmls

Figure 3.1 : Schematic of a standard MBE system

One of the advantage of MBE is the surface of the growing layer can be monitored using in-situ Reflection High Energy Electron Diffraction (RHEED). In this technique a beam of high energy electrons (typically 15-30 keV) is directed on the surface at a glancing incident angle as shown schematically in figure 3.1. The diffracted electrons are then

projected onto a phosphor screen where a camera can record the images. Because of the high energy of the electrons, the corresponding wavelength is < 1Å. As a result the RHEED technique is extremely surface sensitive, typically probing the top one to two monolayers of the growth surface. RHEED can be used to monitor the stoichiometry of some oxide film growth, such as STO. Any deviation from stoichiometry can then be correct by shuttering the relavant sources. In addition, for layer by layer growth the intensity of the RHEED features ocillates during growth with periodicity that corresponds to the growth rate of the film.

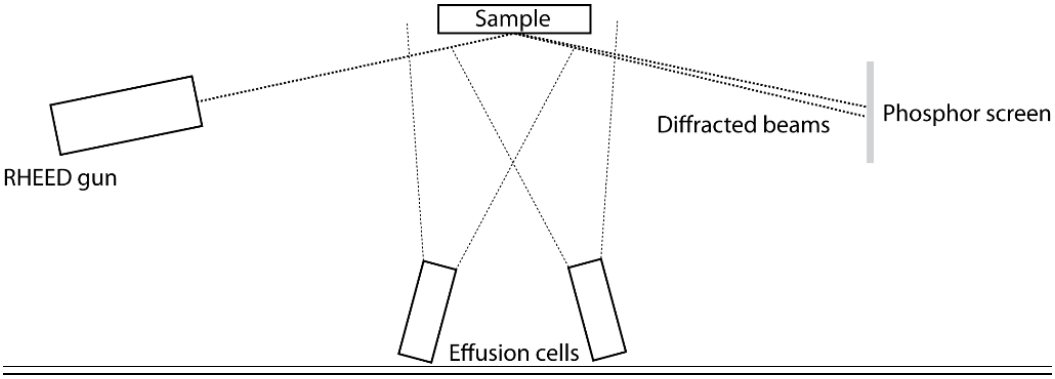

Source: http://www2.warwick.ac.uk

Figure 3.2 : Schematic of a RHEED arrangement within a MBE system.

Chemical Solution Deposition/Spin-Coating

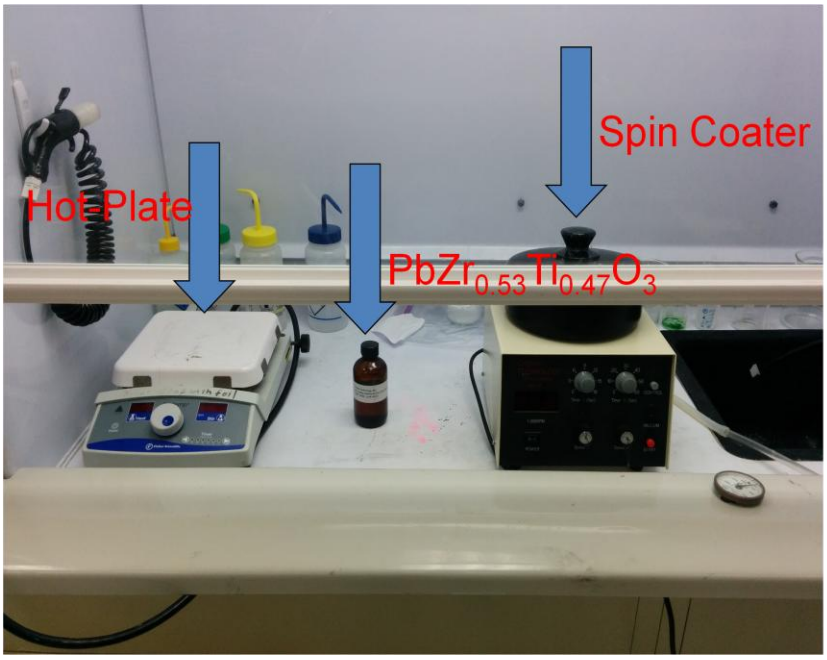

Figure 3.3 : Spin coater used to grow thin films housed within the MBE lab under a fumehood.

Source: http://nl.wikipedia.org/wiki/Spincoating

Figure 3.4: The deposition of a solution onto a substrate mounted to a vacuum chuck in a spin-coater.

Spin coating uses a source material in an alcohol (within this thesis) solution. A spin coater is utilized with two separate stages for rotation. The source material is deposited on a substrate that is mounted onto a rotating chuck and held in place using vacuum. The initial stage uses a low spin speed to spread out (see figure 3.4) the material evenly and

then the second stage with the higher spin speed is for smoothening out the surface. This is followed by a short bake using a hot-plate at a temperature higher than the boiling point of the solvent before being transported for an additional pyrolysis step to discourage formation of organics within the structure. The pyrolysis is then carried at a temperature lower than the crystallization of the source material to ensure that any organics forming do not get trapped within the crystal structure or hinder the crystallization in any manner. A final annealing is performed after the pyrolysis to ensure complete crystallization.

X-ray Photoelectron Spectroscopy

XPS was invented by K.Siegahn and his research group in early 1960s while with University of Uppsala in Sweden. This invention eventually led to his Nobel Prize in 1981 thus highlighting the importance of the technique.

The simplest way to understand XPS is through the idea of photoelectric effect. Photoelectric effect is the one of the modes for generating current using light, currently employed in solar cells using today. The principle behind photoelectric effect involves irradiating a surface with sufficient enough energy to eject electron from a surface such as a metal. This is given by the Nobel Prize winning photoelectric effect equation proposed by Einstein in 1921:

$$KE = hf - \varphi$$

The kinetic energy of an ejected "photoelectron" (KE) is equal to the incident energy (hf) of the radiation minus the binding energy involved in the expulsion of the electron (identified as φ the work function of a material).

The key to the equation is binding energy and it is a unique value. The photoelectric effect may thus be viewed as a way to identify binding energies of a material given that the incident energy and kinetic energies are known. XPS uses a high vacuum chamber wherein a radiation source is directed towards a sample and the ejected photoelectrons are identified by a detector. The scans are usually performed for a range of binding energies typically using Al Kα (1486 eV) rays. Most elemental compositions have their binding energies under 1200 eV and therefore Al Kα is sufficiently large enough to identify most compositions. For every given binding energy there is a specific peak associated with it. For example elemental oxygen in its 1s configuration always occurs around 530 eV.

Those in bound states like that of STO have their oxygen 1s peak slightly shifted away from 530 eV to compensate for the change in binding energy. Oxygen in its 1s configuration has a single peak associated with it. This is due to s orbital having a total angular momentum of 1. However in the case of a p orbital, there is a splitting of energies in the form of $p_{1/2}$ and $p_{3/2}$. This splitting is indicated as two unique peaks (a doublet) occurring close to each other. Thus for a 2p peak in manganese with some oxidation state (2+,3+ etc.) a doublet is observed around 641 eV and 653 eV for Mn $2p_{3/2}$ and Mn $2p_{1/2}$ respectively.

X-ray Diffraction

High angle X-ray Diffraction measurements were performed using a BEDE^{TM} system. All the work carried out is highly dependent on crystallinity and therefore along with RHEED forms a major portion of this work. XRD has been extensively used to determine additional phases and to confirm phase purity in the grown materials. XRD makes use of scattering of an incoming radiation across lattice planes in a crystal. The scattering is governed by Bragg law (figure 3.5).

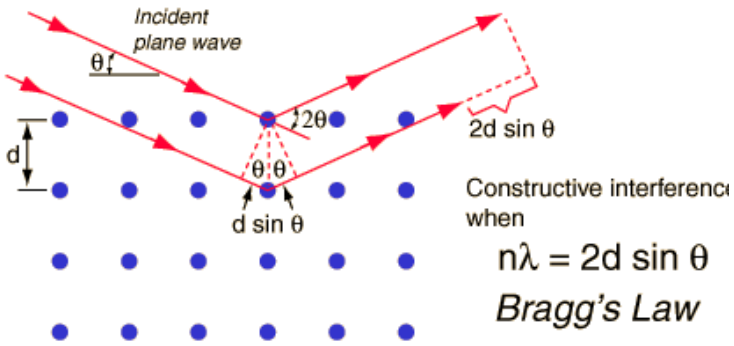

Source: http://hyperphysics.phy-astr.gsu.edu/hbase/quantum/bragg.html

Figure 3.5: Bragg law is shown pictorially. An incident ray at an angle theta is scattered when interacting with a lattice plane. Constructive interference takes place when path difference (d) is an integer multiple of the wavelength (lambda).

The equation states that given a certain angle of incidence for a certain lattice spacing there is a constructive interference of the incident rays. This constructive interference thus forms a peak in an XRD pattern. XRD is performed as a sweep within a window of angles. As dictated by Bragg law each angle of incidence may give a peak or may observe destructive interference depending on the type of material being scanned. High

angle XRD uses an incoming radiation that is swept from a smaller angle to that of a larger angle. XRD patterns for a range of incident angles are unique to different crystalline structures. XRD is thus also used to identify different crystalline phases in non single crystal growths. Most of the data presented in the thesis has their XRD patterns swept for a 2theta from 10^o to 75^o.

Ferroelectric Hysteresis

All ferroelectric measurements were performed at Penn State University using a TF 2000 piezoelectric analyzer. The set-up uses a simple Sawyer-Tower circuit. The material is swept through a range of voltages and the net polarization is measured using charge integration. The hysteresis is performed by using 1 KHz sawtooth waveform sweeping from 0 V to 10 V, -10 V to 10 V and 10 V to 0.

IV. $BiMnO_3$ ON $SrTiO_3$/Si

Introduction

Manganese's unique feature is its ability to take on a variety of oxidation states ranging from +0 to +7. This feature gives it an extreme amount of flexibility when creating new compounds or modifying existing compounds for additional valance states under a Landau-type phase transition effects [10]. As was earlier shown, breaking inversion symmetry and exchange mechanism are the primary means of ferroic orders of electricity and magnetism in perovskite oxides. Hence incorporating manganese within a versatile structure such as a perovskite has been shown to be both theoretically and experimentally viable [10][7][8]. Manganese based perovskites exhibit some very interesting functionalities. These are unique in the sense that most of the so called multiferroics belong to this category. These are materials where we have coexistence of ferroelectricity and ferromagnetism ($TbMnO_3$, $LaMnO_3$ and $BiMnO_3$)[10]. The possible applications with this kind of coexistence are limitless; we can build very accurate sensors, low powered data storage and even double our storage density in hard drives. Other uses include, but not limited to, that of future energy generation using Solid Oxide Fuel Cells, possible superconductors and Colossal Magnetoresistance for memory applications [10][7][6].

Brief History

Earliest works on thin film BMO was carried out theoretically by Nicola Hill in 1999[39] and Ram Seshadri in 2001[40], giving us the necessary background for origins of ferroic orders of magnetism and electricity along with multiferroism. However it was not until Pulsed Laser Deposition (PLD) growths by Schlom *et al* in 2004 [41] that thin film growths of BMO were carried out, giving experimental proof for ferroelectricity and ferromagnetism. MBE growth of BMO was not carried out until 2010 by Schlom *et al* [42]. Our growths are partially based off on this work. The primary differences with growth by Schlom's group and our growths are the following:

a. Schlom used STO [100] as a substrate; however we used STO/Si virtual substrate.

b. Growth was carried out in an ozone environment to possibly facilitate easier growth of BMO whereas in this study molecular oxygen was used. This is due to the fact Schlom's paper on MBE growth of BMO remains to be the only MBE work on BMO. Our work primarily provides a means to grow epitaxial BMO thin films on a silicon substrate for "more-than-Moore" type functional integration onto current semiconductor device technologies.

Functionality

BMO observes a distorted monoclinic C2 non centrosymmetric structure and belongs to the perovskite oxide family [39]. Its structure is described in figure 4.1, viewed from

[111] direction , below with bismuth, manganese and oxygen represented by white, blue and red balls respectively.

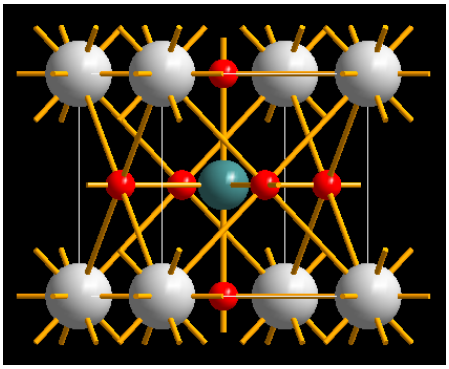

Figure 4.1: An ideal cubic perovskite structure.

Unlike other manganites ($YMnO_3$, $HoMnO_3$, and $TbMnO_3$) that exhibit antiferromagnetic behavior, BMO exhibits ferromagnetism. The ferroelectricity in BMO is driven by stereochemically active lone pair from $6s^2$ in Bi. This lone pair causes octahedral distortion of MnO_6 via the second order Jahn-Teller effect and therefore effectively breaking inversion symmetry [40]. The lone pair effect also leads to distortion in Mn-O-Mn bond angle and via the Dzyaloshinskii-Moriya interaction gives rise to ferromagnetism [40][43]. Therefore it can be said that both the ferromagnetism and ferroelectricity in BMO arises from lone pair mechanism. In addition, these properties also enable BMO to be multiferroic.

Growth

BMO growth starts with a single crystal p-type silicon substrate oriented in the [100] direction. Growth was performed using Molecular Beam Epitaxy (MBE) in an oxide dedicated chamber. A initial layer of STO, thickness around 5nm, was grown on silicon

to act as a virtual substrate for BMO growth. Theoretical work involving the enthalpy of formation for BMO from Bi_2O_3 and Mn_2O_3 yields a value of 4000 J/mol on the higher end. The substrate temperature was therefore increased to 710^{o}C, after several unsuccessful attempts, from an earlier 550^{o}C (used for STO growth) to compensate for the added requirement for energy. The growth was performed with excess Bi flux because of its high vapor pressure. To ensure the correct stoichiometry superlattice of MnO_2 and BiO was grown using an oxygen over-pressure of 2 x 10^{-6} torr. Bi and Mn were shuttered for 15 and 10 seconds respectively with oxygen always on. The times were chosen by examining the RHEED patterns to ensure that the surface does not degrade. The shuttering was performed over 90 loops for a total of 2250 seconds. Temperatures for Mn and Bi effusion cells were calibrated for 1050^{o}C and 573^{o}C respectively.

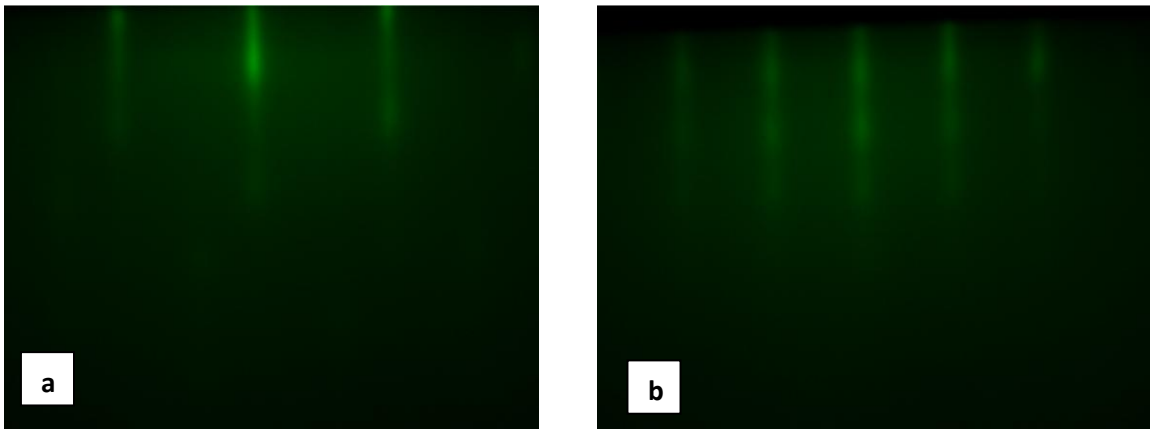

Figure 4.2: a) [210] azimuth for BMO growth, b) [110] azimuth for BMO growth

RHEED was used to monitor crystalline quality of the growths. The figure 4.2 (a and b) shows RHEED patterns for [210] and [110] azimuths respectively at the end of BMO growth. The patterns indicate a successful epitaxial integration of BMO on STO/Si

surface. This can be discerned from $SrTiO_3$ RHEED pattern in figure 4.3 at the end of its growth to that of the BMO growth from figure 4.2.

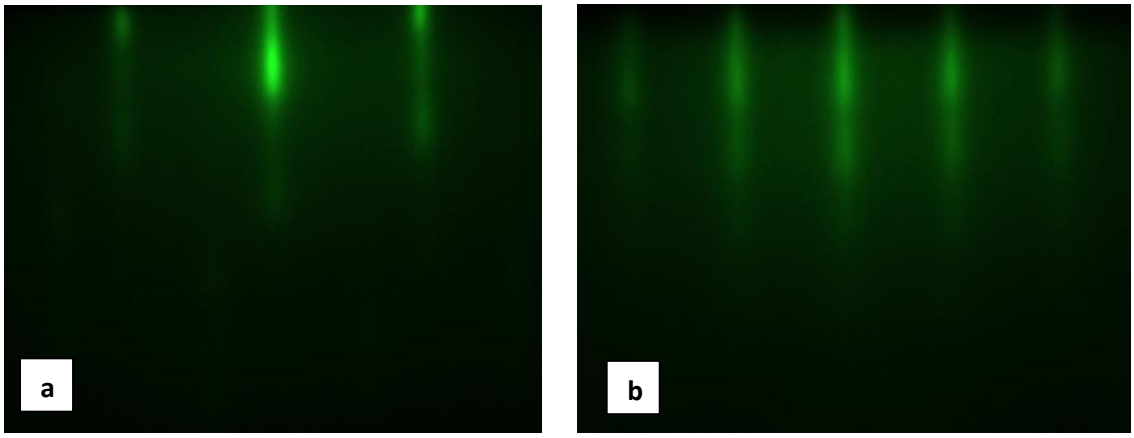

Figure 4.3: a) [210] azimuth for STO growth, b) [110] azimuth for STO growth

X-ray Photoelectron Spectroscopy

To determine whether BMO has successfully grown on STO/Si, XPS was performed *in-situ* after the growth to identify bonding states and the chemical integrity of the topmost layer. An initial survey scan was performed to check for peaks and this was followed by window scans of individual elements for added information with bonding behavior. The survey is shown in figure 4.5 and the elemental window scans are shown in figures 4.4 (a, b, and c). The spectra suggest that the film contains Mn, Bi and Oxygen. In addition, since the presence of Sr and Ti are also detected, it can be assumed that the thickness is less than 3nm

All the XPS data was analyzed using AAnalyzer software. Oxygen 1s peak indicates the presence of BMO at 532.2 eV [44], in addition to STO at 530 eV. Both the Mn and Bi peaks show single oxidation states. The absence of additional oxidation states

demonstrates a phase pure growth with complete oxidation. In combination with RHEED analysis, structural and chemical purity is established. The survey scan was earlier used to identify elemental peaks (as shown in figure 4.5)

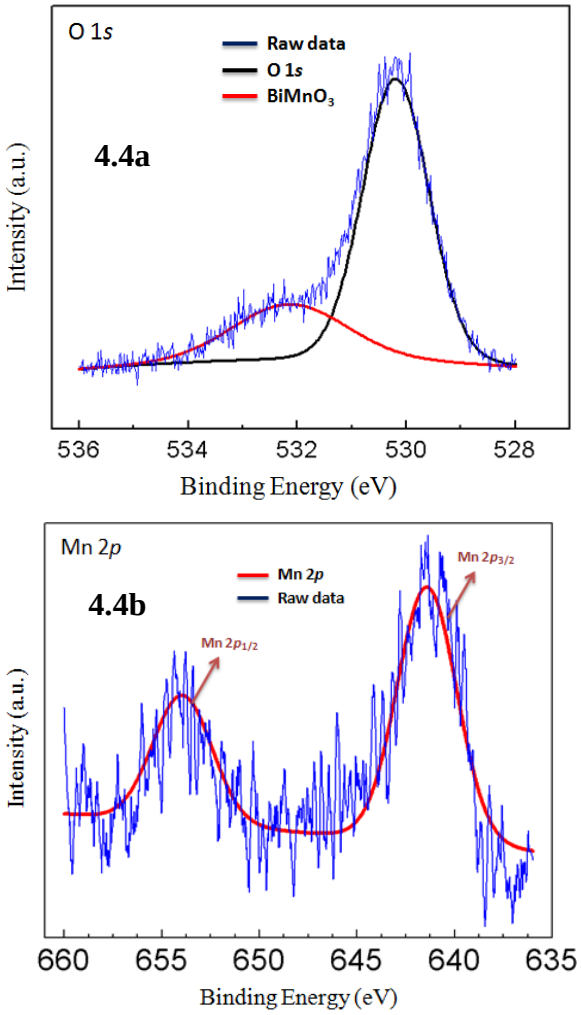

Figure 4.4: XPS fits for a) O 1s peak, b) Mn 2p and c) Bi 4f

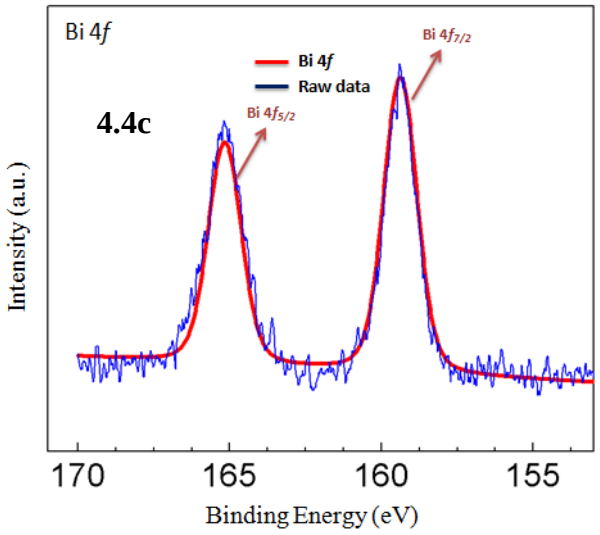

Figure 4.4, continued here

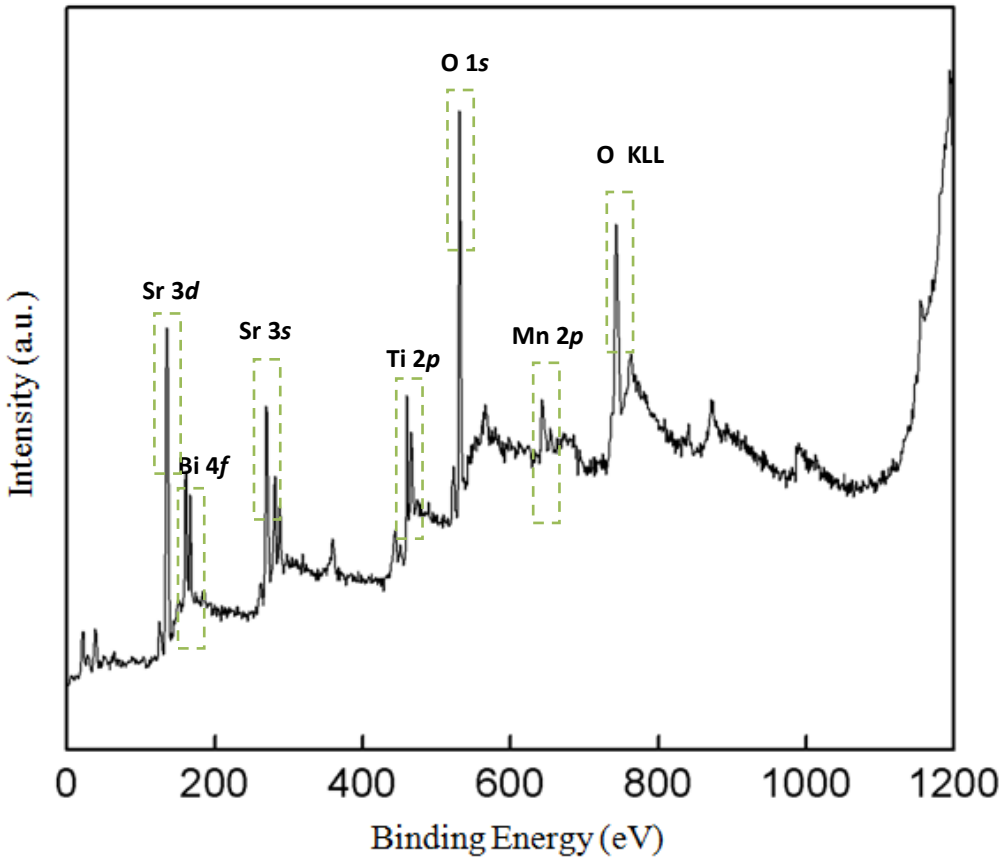

Figure 4.5 : XPS survey scan indicating Sr, Bi, Ti, O and Mn peaks.

X-ray Diffraction

High angle XRD scan was performed to confirm structural morphology, obtained earlier from RHEED, and also to check for phase purity of the growths. Single crystal perovskite oxide grown along [100] direction indicates very distinctive peaks at 23.4^{o} (001) and 46.5^{o} (002) in the plot. The plot also carries the prominent Silicon (004) peak at 69.5^{o}.

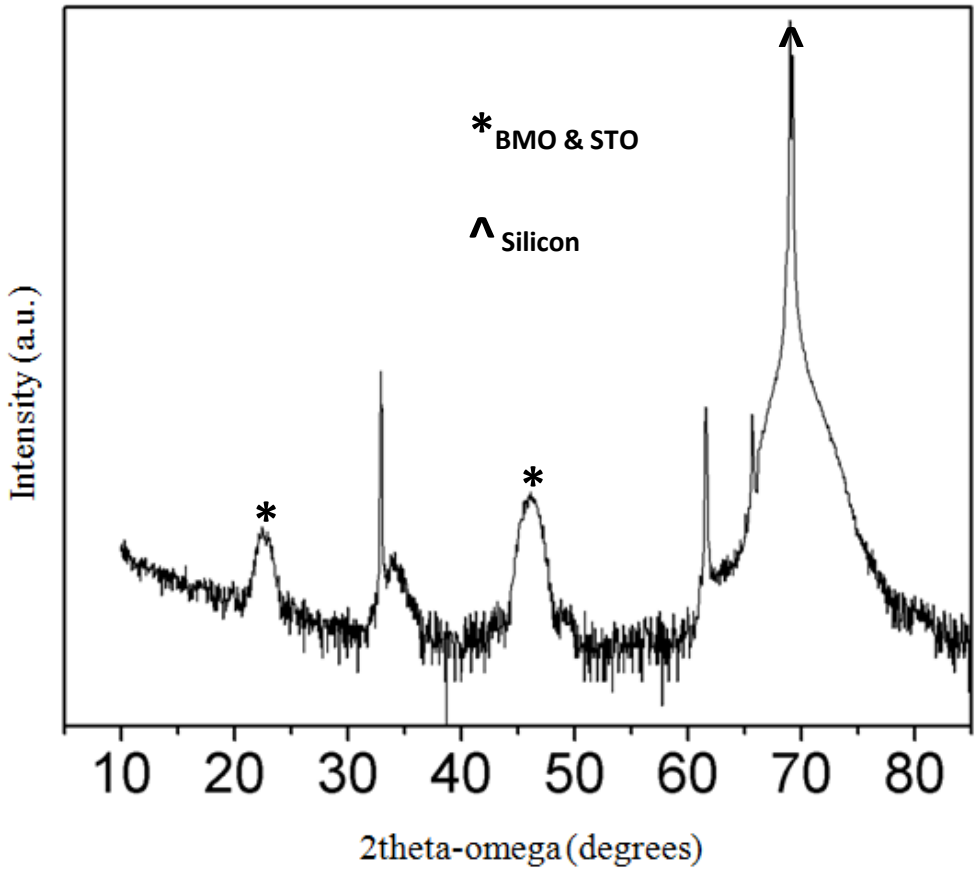

Figure 4.6 : [High angle] XRD scan for BMO on STO/Si

STO and BMO when rotated at 45^{o} , with respect to Si, carry a-site parameters of 3.905 Å and 3.90 Å respectively[42]. This gives them a low lattice mismatch of around 1%..

With the films being grown ultra-thin and the lattice mismatch being close, we expect to not observe any significant interfacial strain between STO and BMO and therefore no peak splitting is indicated from the high angle XRD patterns either. Therefore, both the STO and BMO occur at the same angle indicating epitaxial growth.

V. $PbZr_{0.53}Ti_{0.47}O_3$ ON Si AND $SrTiO_3$/Si

Introduction

PZT is an excellent piezoelectric material currently in extensive use in the field of sensors memories and actuators [45][46][47]. It's also a pyroelectric material finding use in infra-red imaging [45]. There has been great interest in MEMS devices. MEMS is the creation of nanoscale devices performing physical work to create smart products that can sense and respond in very small scale environments such as microsensors and microactuators[45][46][47]. With this integration, the MEMS devices can receive and relay information through the circuitry that's already in place for more intelligent functionality. In addition PZT is a ferroelectric material. It therefore has been effectively used in DRAM and FeRAM applications [11]. Recent research has drawn attention to Metal-Ferroelectric-Insulator structures (MFIS) [48][49][50]leading to a FERROFET device that utilizes the ideas of negative capacitance to reduce the sub threshold slope of transistors to below 60mV/decade [51][52][12] for ultralow power operation. PZT's high polarization coupled with its piezoelectric and ferroelectric ability has encouraged its extensive study however lead is environmentally unfriendly and is therefore highly undesirable for large scale applications. Given the versatility of PZT, it can be used extensively in laboratory conditions to test for ideas thus serving as a "proof of concept" vehicle. In our current study, we are primarily concerned with growth and optimization of PZT on $SrTiO_3$/Si substrate and the ability of PZT to retain ferroelectric behavior in the

end product. This would therefore enable for further study of ferroelectric oxide based devices including FERROFETs.

Brief History

Jaffe et al. [53] was the first to report the existence of a Morphotropic Phase Boundary (see the following section) in PZT that caters towards increased polarization in the solid solution. Therefore the focus was shifted from $PbTiO_3$ and $PbZrO_3$ perovskites, both ferroelectric, to that of a solid solution between them. Initial growths were performed using chemical solution deposition (CSD) or spin coating [54] and physical vapor deposition methods. Non CSD growth techniques such as PLD, RF sputtering and MBE have been implemented extensively [55]. These techniques utilize high vacuum conditions and are therefore far more expensive than a CSD route. CSD continues to play a major role, primarily due to the cost involved and also the ease of crystallization for a highly oriented PZT. CSD also facilitates a uniform growth and in the right conditions gives an increased control over the stoichiometry of the material deposited. The net polarization in PZT is highly phase dependent and therefore is stoichiometry sensitive [47] [56]. The primary disadvantage of CSD and the advantage high vacuum type growth has to do with device fabrication. It is highly difficult to achieve nanoscale devices with CSD due to its increased difficulty to produce ultra-thin (<30 nm) films and therefore techniques such as PLD and ALD are on the rise to facilitate PZT integration onto current silicon technology.

Mechanism

PZT is a perovskite structure with Ti and Zr alternatively forming the centers of an octahedral ZrO_6 and TiO_6 network surrounded with cubic Pb arrangements. It observes both tetragonal and rhombohedral structure as shown in figure 5.1. Under an applied electric field the d^0 configurations for Ti^{4+} and Zr^{4+} observe a distortion (Second order Jahn Teller) shifting towards one of the oxygen atoms [47]. This is a hysteretic effect and is therefore a ferroelectric material. The structure of PZT is same as the one described earlier in chapters II and IV and in addition is shown in figure 5.1 along the [111] plane direction.

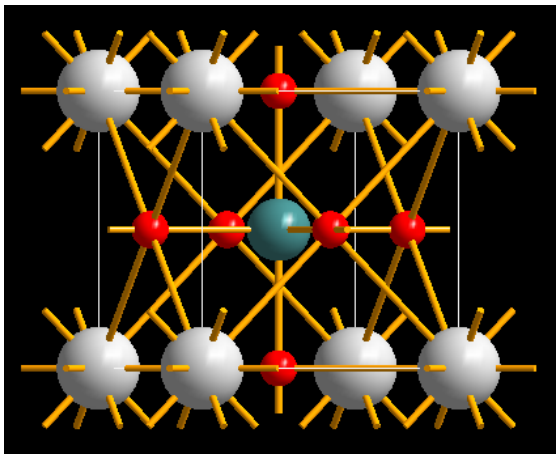

Figure 5.1: An ideal cubic perovskite is shown. In the case of PZT the central atom (shown as a blue sphere) is alternated between Zr and Ti ions within the oxygen clusters (shown by red spheres). The white spheres are either Zr or Ti depending on the central atom being Ti or Zr.

Morphotropic Phase Boundary

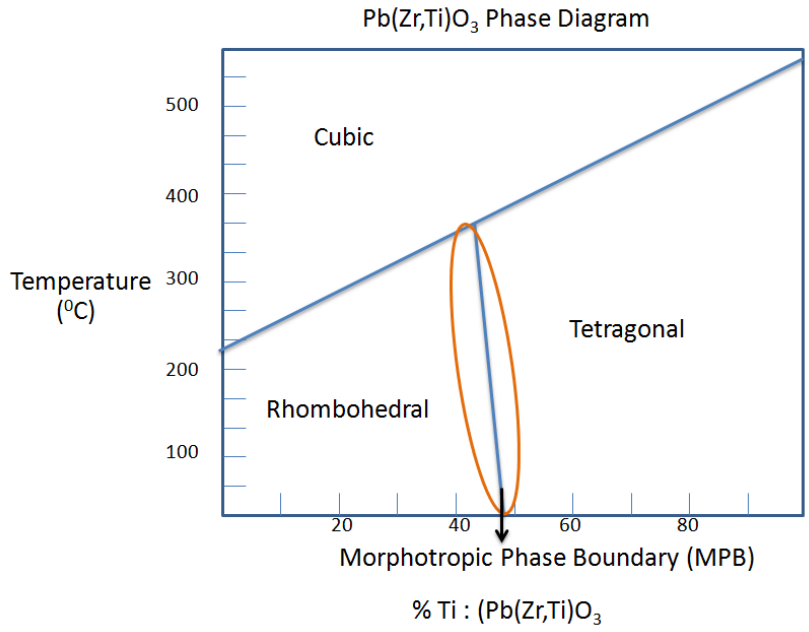

Figure 5.2: Phase diagram for PZT is shown indicating the MPB at the transition point of Rhombohedral and Tetragonal phases.

The growth and properties of PZT are highly governed by Ti:Zr ratio in its stoichiometry. As is shown in figure 5.2 modified from Jaffe et al. [53], the Ti (or Zr) concentration in PZT gives rise to a very specific crystal structure. Both the rhombohedral and tetragonal are conducive for a ferroelectric perovskite structure. However, it is known [53] that a concentration around the MPB occurring at the transition from rhombohedral to tetragonal leads to the highest polarization in PZT. The cause for it, as explained by Jaffe et al. [53] and then later elaborated by Isupov [57], has its origins in increased polarization orientation directions. A Tetragonal phase has six possible directions and a rhombohedral structure has 8. At the MPB both these phases coexist, giving rise to a net 14 directions for the orientation and therefore an increased net polarization. It was due to

this reason that our source material for PZT has the structure of $Pb_{1.1}Zr_{0.53}Ti_{0.47}O_{3,}$ and as can be seen in the figure, the titanium with a 47% composition occurs right at the MPB. The reason for excess lead in the formula is discussed in the next section.

Growth

CSD growths were carried out in a spin-coating machine housed within the MBE lab under a fume hood. The source was obtained from Chemat Technologies with the chemical formula $Pb_{1.1}Zr_{0.53}Ti_{0.47}O_3$ in a 2-methoxyethanol solution. The primary concern with PZT growth, as referenced from earlier sources [55][56], is the temperatures involved with intermediate baking and annealing. Another major issue when growing PZT is to sustain the right stoichiometry at the end of any growth process. All solution based growths require some type of annealing mechanism. It has earlier been shown [55][58][59] that PZT observes an excessive loss of Pb via PbO formation during the baking process therefore we have used a source material with excess lead to counteract the loss. However, lead loss can still occur if a pyrolysis step is not undertaken [59] leading to the formation of, the highly undesirable, non ferroelectric (at room temperature) pyrochlore ($Pb_2(Zr,Ti)_2O_7$) or a fluorite type phase ($Pb_2(Zr,Ti)_2O_{7-x}$)[58][46].

The growths were performed using two distinct routes. The first is the easier, with a hot-plate for all our baking and annealing steps. However this route completely disregards the requirement of a pyrolysis step since any pyrolysis step, by definition, requires a vacuum or an inert environment using noble gases such as argon. The second process is more involved and time consuming using a two-stage tube furnace. This route gives us the

advantage of creating any environment we desire since we can hook-up any gas source to the tube during annealing or even create vacuum if needed. A more detailed explanation and results using the two processes is given as follows:

Hot-plate

The first and the easiest was the hot-plate route. This is described in the flow chart (figure 5.3) below:

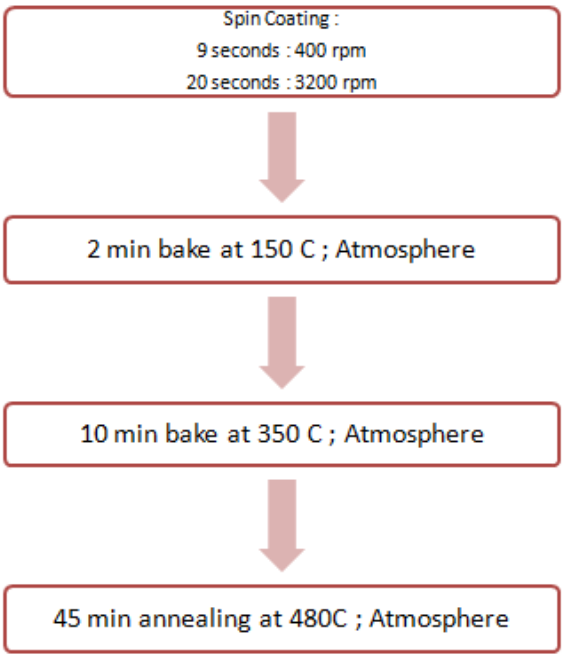

Figure 5.3: Flow chart for PZT growth using hot-plate as heat source.

The major concern with this growth is the 10 min intermediate bake at 350^{o}C taking place in atmosphere conditions. We were also limited by the hot-plate's ability to reach the preferable temperature of 600^{o}C for perovskite phase PZT formation [58]. It is recommended to use a pyrolysis at this stage to discourage formation of organic molecules due to the 2-methoxy ethanol serving as a solvent for the PZT. An XRD

example is shown in figure 5.6 (middle) indicating the presence of a variety of peaks in addition to the standard perovskite phase peaks. These peaks relate to both the pyrochlore and fluorite phase. However, an increased annealing time has shown to decrease these additional phases effectively. The XRDs for these have not been shown here for the primary reason that the presence of the ferroelectric perovskite phase is considerably lower than the tube-furnace growth. The ferroelectric hysteresis data in the characterization section indicate this drastic change.

Tube-Furnace

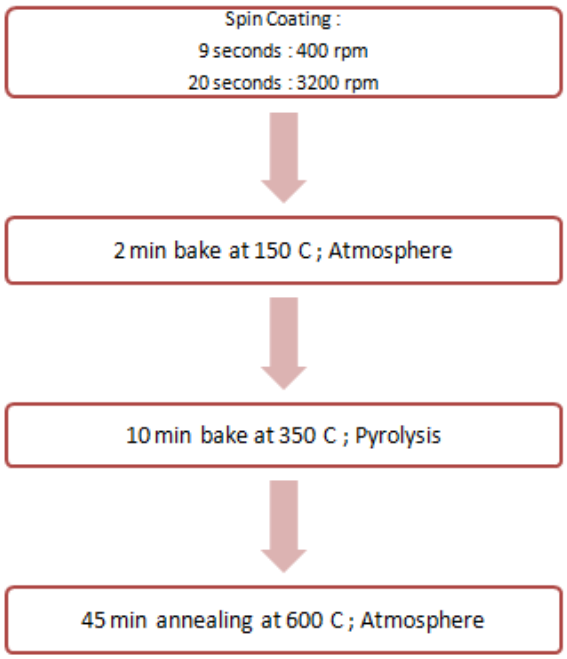

Figure 5.4: Flow chart for PZT growth using tube furnace as heat source.

The tube furnace growths were performed in a Lindberg furnace with three stages for heating. The sample was prepared the standard way (as indicated in figure 5.4) with a spin coater and baked for a minute before being transported to the tube furnace. The

pyrolysis was carried out in an excess argon environment at 350^{o}C. Results from other groups using TGA/DTA analysis [58][60][61] showed PZT crystallization starts around 400^{o}C with a higher temperature of around 600^{o}C being a favorable temperature for perovskite phase PZT formation. The temperature optimization was finalized after several growths performed from 550^{o}C- 700^{o}C range and tested for structural morphology. The results from XRD and ferroelectric hysteresis both indicate that a highly oriented (100) perovskite phase PZT can be produced most effectively using a tube furnace with a temperature around 600^{o}C - 620^{o}C.

X-ray Diffraction

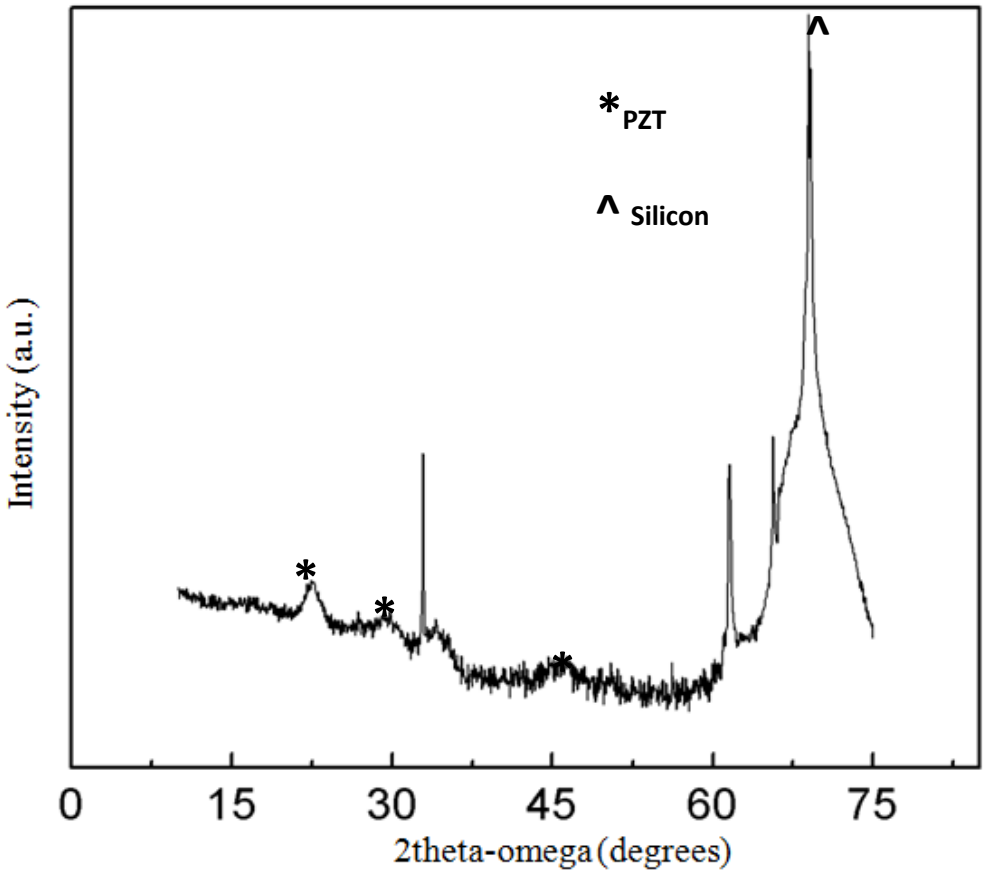

Figure 5.5: XRD plot for PZT grown on Si substrate with no seed layer.

The figure 5.5 is that of PZT grown on bare Si without a STO seed layer. Our initial assumption was that the growth would indicate a multitude of phases due to a lack of proper seed layer. However the plot clearly shows a PZT taking a perovskite structure. The key nonetheless with this picture is when compared with XRD plots containing STO as a seed layer the growth using a Si substrate has diminished level of crystallinity.

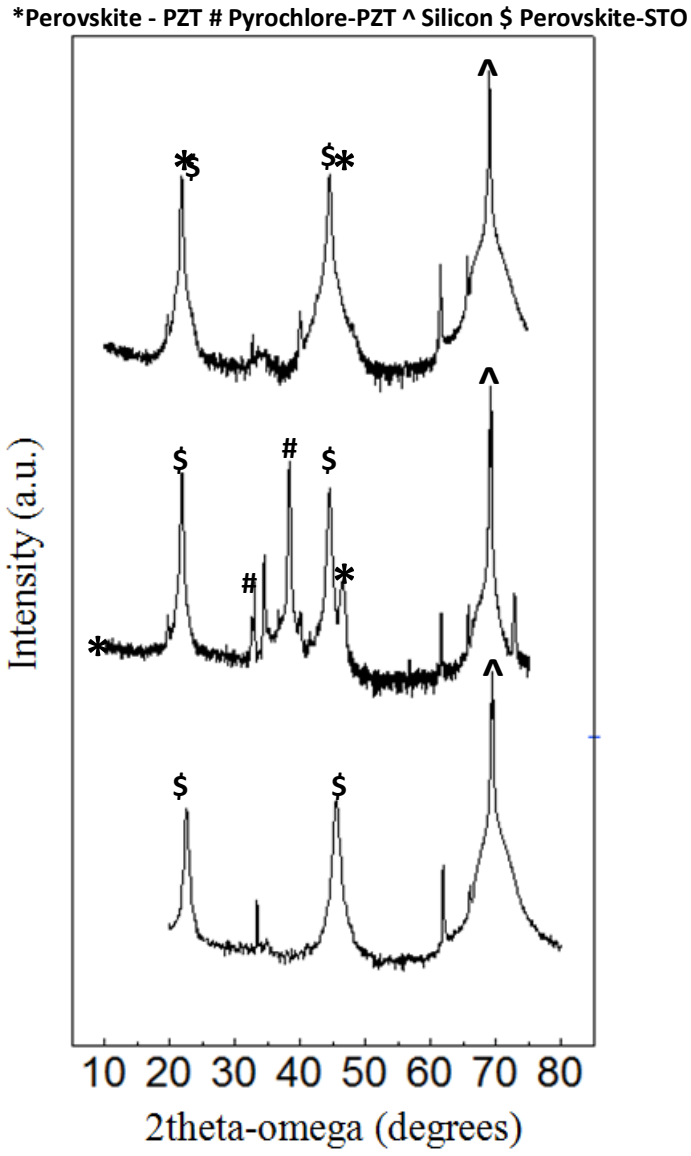

Figure 5.6: XRD scans showing PZT deposited on STO/Si (top), Pyrochlore-rich PZT on STO/Si and STO/Si

The XRD plots shown in the above figure (figure 5.6) demonstrate growth of PZT on STO/Si. Plots with virginal STO on Si is shown at the bottom whereas the PZT grown STO on Si is shown at the top. Visually there is no remarkable change. Epitaxial STO was grown on silicon in the [100] direction. We therefore have used a highly oriented seed layer in the form of STO. PZT plot indicates the growth of PZT along this orientation conforming to a single crystalline perovskite phase pure material. The standard perovskite peaks are identified at 23.4^{o} (001) and 46.5^{o} (002). The peak 69.5^{o} is Silicon (004).

Atomic Force Microscopy

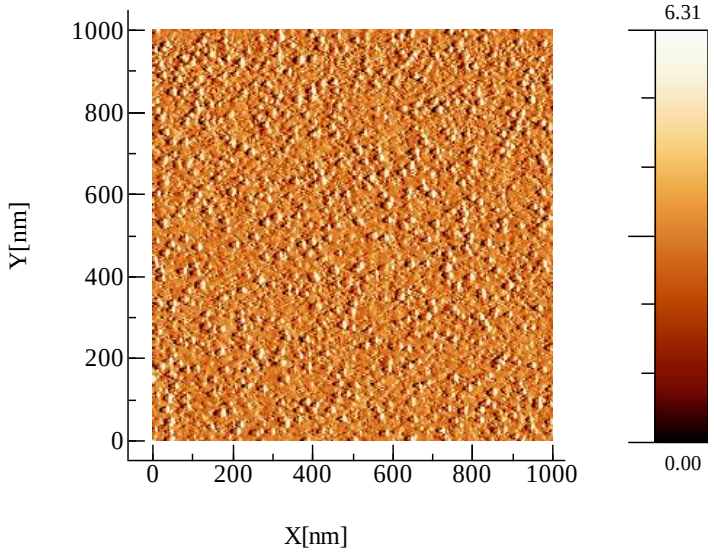

Figure 5.7: AFM image for PZT deposited on STO/Si indicating large number of nucleation sites.

Roughness analysis was performed on tube furnace growths of PZT using STO seed layer on Si and compared against that done on Si substrates. A roughness of 1.4 nm was

measured for PZT grown on a Si substrate with an STO seed layer. The area measured was 1 µm X 1 µm. This is given in figure 5.7. In addition the figure also shows a network of islands possibly indicating crystalline PZT.

The growth for PZT grown on Si substrates shows a roughness of 7.3 nm in an area of 5 µm X 5 µm. figure 5.8 shows the AFM measurement. The surface in comparison with figure 5.7 shows lack of any island growths. These results when put together within the context of those obtained from XRD show that the islands within figure 5.7 are likely perovskite rich regions and contribute to overall crystallinity and the absence of these in figure 5.8 conforms to the XRD plot showing a subdued crystalline presence.

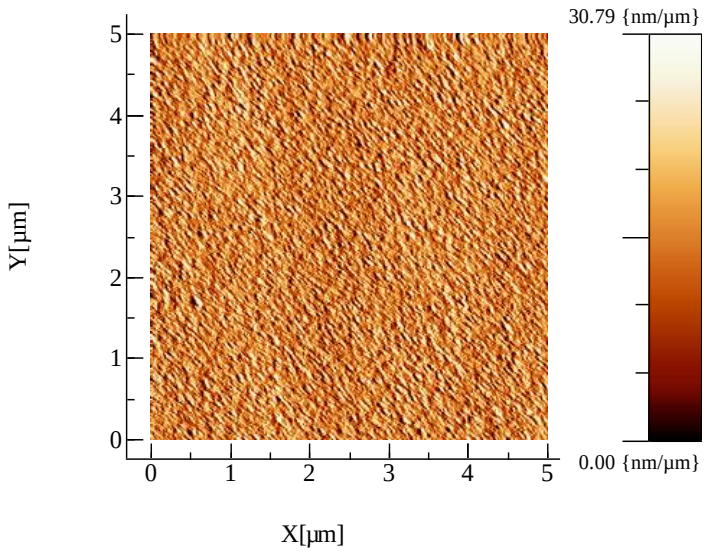

Figure 5.8: AFM image for PZT grown directly on Si. Diminished island formation indicating a lack of nucleation sites when compared to Figure 5.7

Ferroelectric Hysteresis

Figures 5.9 and 5.10 represent polarization curves aka hysteresis for pyrochlore rich PZT and perovskite rich PZT respectively. The pyrochlore rich PZT is almost twice lower than the perovskite rich PZT in its peak polarization.

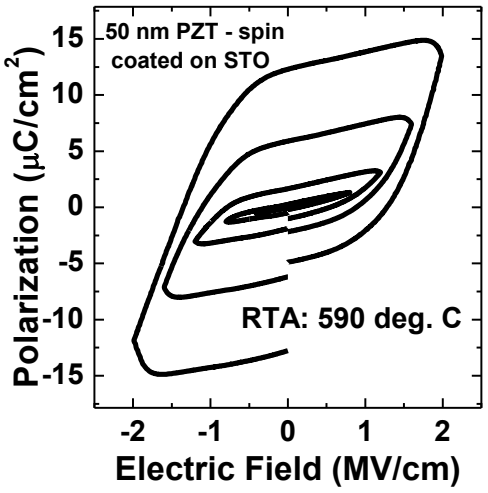

5.9

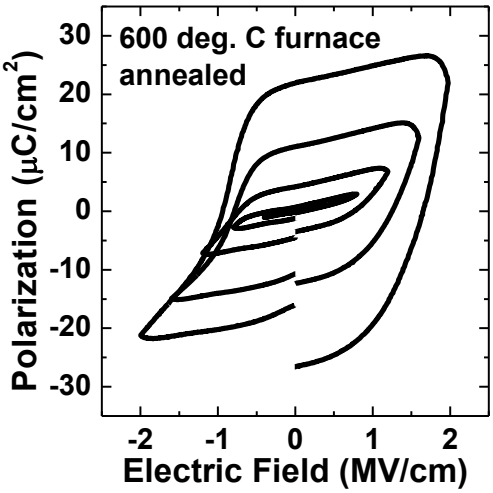

5.10

Figures 5.9 and 5.10: P-E curves for pyrochlore rich (5.9) and perovskite rich (5.10) PZT grown on STO/Si indicating ferroelectric hysteresis.

With a remnant polarization of 25 μC/cm^2, perovskite rich PZT data is comparable with other groups growing on an STO seed layer substrates. A sharper edge in a hysteresis curve indicates complete saturation and this is observed more so within the perovskite phase than the pyrochlore phase data. A standard hysteresis is derived from Landau theory of phase transitions and concerns purely with polarization arising from the ferroelectric material itself. Any curved edge in a hysteresis curve thus exhibits added polarization not from the ferroelectric process within a material. This maybe attributed due to the charge leakage due to additional phases by non-ferroelectric phases or even

from the device itself. Charge leakage is also observed the difference in polarizations at the beginning and the ends. This is significantly diminished in the plot for perovskite rich PZT. However neither of the plots is close to a standard hysteresis plot with high symmetry. Therefore more work needs to be done to improve crystallinity and along with it significantly reduce any contribution from pyrochlore type non ferroelectric phase.

VI. LEAD-FREE FERROELECTRICS ON Si AND $SrTiO_3$/Si

Introduction

Lead-free ferroelectric (back then, prior to 1960s, they were simply ferroelectric oxides) oxides have been a focus long before PZT proved to be a potent material [47]. All this has its beginning with the first ferroelectric material, Rochelle salt discovered in 1921 [17]. However it was not until 1941 [62] with the synthesis of $BaTiO_3$ that ease of device applications was demonstrated. BTO continues to remain a popular lead free alternative to PZT. There have been several other alternatives proposed over the last 40+ years since PZT was identified as an excellent piezoelectric [63]. The most common are those within the perovskite class of materials carrying the ABO_3 structure. Some common materials under this category are $BiFeO_3$, $LiNbO_3$, and $BaTiO_3$ along with these there are plenty of substituted systems containing quaternary and higher compositions similar to $(Bi_{1/2}Na_{1/2})TiO_3$, $Bi_{1/2}K_{1/2}TiO_3$ and $K_{1/2}Na_{1/2}NbO_3$[63][64]. Layered compounds using bismuth oxide (or a metal oxide) form the next most popular group of lead free ferroelectrics. These take the structure of (Bi_2O_2) $(A_{m-1}B_mO_{3m+1})$ or (Me_2O_2) $(A_{m-1}B_nO_{3m-1})$ with A and B site being metal atoms respectively. Examples of this group include $Bi_4Ti_3O_{12}$, $SrBi_4Ti_4O_{15}$ and $KSr_2Nb_3O_{10}$ [65]. In addition there is the boracite family that has shown great promise with the formula $M_3B_7O_{13}X$, here M is a bivalent cation and X is a monovalent anion [14]. Examples within the boracite family include the first multiferroic boracite $Ni_3B_7O_{13}I$, $Co_3B_7O_{13}Cl$ and $Ni_3B_7O_{13}Br$. There are plenty of other lead free ferroelectric options not part of the oxide family with the most prominent

belonging to the fluoride family as clarified by Scott [66] in his indirect counter paper to Spaldin [9].

This work involves two promising lead free ferroelectrics $LiNbO_3$ and $Bi_4Ti_3O_{12}$ belonging to the ABO_3 and layered bismuth families. A more detailed and focused exposition is given in the following section.

Brief History

LNB

Lithium niobate is special among ferroelectrics. Its use is across a variety of disciplines [67]. All ferroelectrics are intrinsically piezoelectric, pyroelectric and are also optically active. However rarely any ferroelectric possess all these properties with abundance in a single material. LNB is one of the rare materials among ferroelectrics with a multitude of properties. It has high electro-optic, piezoelectric and pyroelectric coefficients [68]. It is also highly optically active material with extensive applications and proven track record in the field of photovoltaics, wave guides, surface acoustic wave devices, electro-optics and photorefractive devices [67][69]. It has a high spontaneous polarization of ~70 $\mu C/cm^2$ and a Curie temperature of around 1200^oC, it is classified as a high temperature ferroelectric [70][71]. Unlike other ABO_3 structures discussed within the thesis, LNB is not a perovskite. It belongs to the 3m point group, which lacks inversion symmetry, and carries a HCP configuration as shown in figure 6.2[67]. Its structure is part of the Ilmenite family which includes other similar oxides such as $FeTiO_3$.

LNB was first synthesized in 1949 by Matthias and Remeika [72] while working at Bell Labs. Earliest solution based growths were performed by Hirano in 1988 [73]. The most

preferred methodology for LNB growth is pulsed laser deposition. Information on LNB growth on silicon is plentiful however the approach of using a high-k dielectric such as STO as a seed layer is sparse. Considering CSD is cheaper and easier to work with, it makes for an excellent way to do proof of concept testing. Within this work, the primary motivation was that of integration of LNB and BIT onto Silicon substrates using STO as a seed layer. The purpose of the seed layer is similar to that of using the same in PZT growths. A seed layer helps with crystallization along a unique orientation giving rise to uniform structure. Another application is to have a FERROFET type device within the category of MFIS type structures [74] [75] [48].

BIT

BIT was first identified by Aurivillius and hence has its structure, even though being a derivation of perovskite is, classified as Aurivillius type. However it was not identified as a ferroelectric until Subbarao described it in 1961 [76] [77]. BIT forms part of a class of bismuth layered compounds with the generic formula (Bi_2O_2) $(A_{m-1}B_mO_{3m+1})$ and the more standard layered compounds are with the formula (Me_2O_2) $(A_{m-1}B_nO_{3m-1})$ [65]. There have been over 50 layered compounds now identified as ferroelectric. BIT nonetheless continues to be a prominent member among those identified. It has a curie temperature of 680^oC [77] with a spontaneous polarization reaching ~50 $\mu C/cm^2$ [78] [79]. It is dubbed as a layered perovskite belonging to the orthorhombic family with octahedral TiO_6 structures embedded between Bi_2O_2 layers [77]. Its decent spontaneous polarization and high dielectric constant makes it a viable candidate for a true replacement of PZT based devices [64] [63] [47] [65]. The structure is indicated in figure 6.3.

Growth

The source materials for both LNB and BIT were obtained from Chemat Technologies as solid solutions with 2-methoxyethanol as a solvent. Growths for both LNB and BIT were carried out using the same formulation as PZT, given in the following flow chart (figure 6.1):

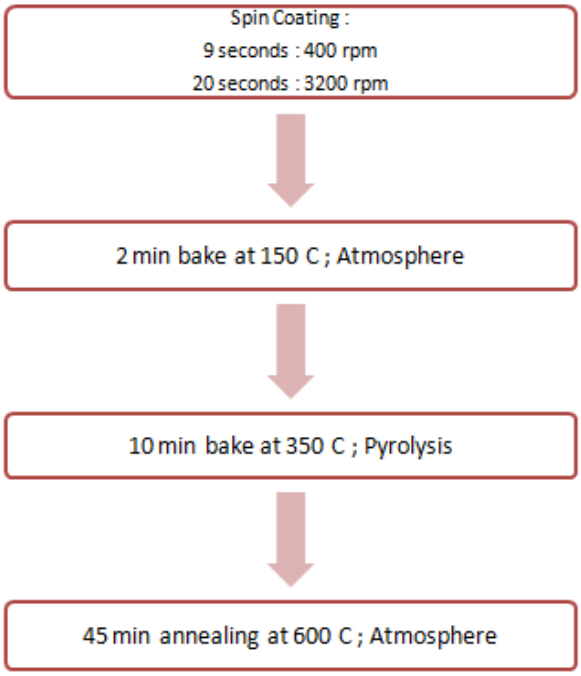

Figure 6.1: Flow chart for both LNB and BIT growths on STO/Si substrates.

TGA/DTA analysis from various growth groups [80] [81] indicates a similar window to that of PZT hence it was decided to stay with the earlier methodology. LNB has a window with crystallization occurring from 600^{o}C to 700^{o}C whereas BIT has a slightly larger window from 550^{o}C to 750^{o}C. TGA/DTA merely gives information as to the point of stability when a material is exposed to heat. It does not establish the change in phases after the stability. It therefore is the task of the experimentalist to determine the right

temperature for the right phase for crystallinity (There is always a room for improvement when optimizing temperature related growths).

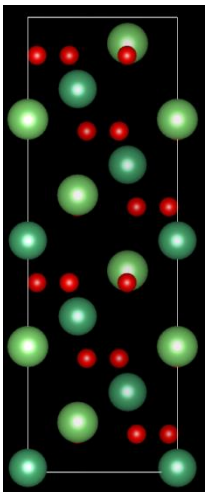

Figure 6.2: LNB crystal structure is described using light green spheres to show Li atoms, dark green for Nb and O atoms are indicated by red spheres.

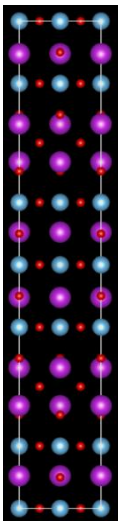

Figure 6.3: BIT crystal structure is shown using purple spheres for Bi, blue for Ti and red for O.

X-ray Diffraction

High angle XRD was performed for growths on (100) oriented STO/Si and Si substrates. Each growth is shown in the figures indicating two different plots stacked together. In each of the stacked images, the top image is growth of source material on STO/Si substrate whereas the bottom half is a test growth performed on Si substrates. This is done primarily to demonstrate the need for a seeding agent like STO.

As can be seen in the figures 6.4 and 6.5, both BIT and LNB show increased activity in their plots when growths were performed using the seed layer. These enhanced peaks

correspond to the perovskite peaks associated with STO indicating a sucessfull epitaxial growth of highly oriented source material.

BIT

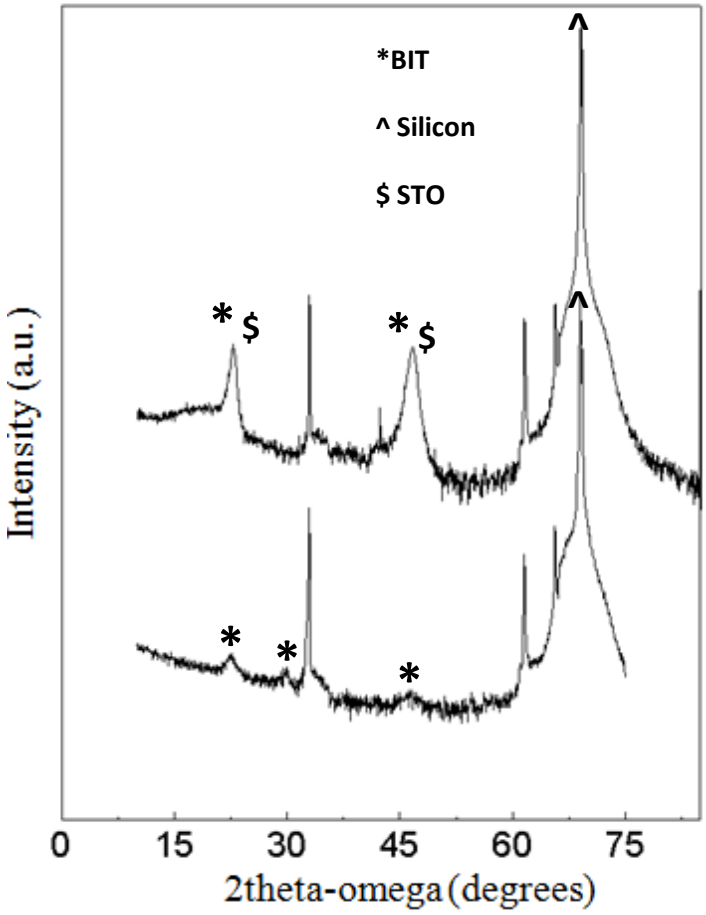

Figure 6.4 : Plots for BIT grown on Si (bottom) and STO/Si (top) are shown.

The lower plot of the stacked images in figure 6.4 shows BIT grown on silicon. This plot in comparison to top image indicating BIT grown on STO/Si substrate clearly shows lower degree of crystallinity. Other than the standard silicon peak (004) at 69.5^{o} there are peaks corresponding to an orthorhombic BIT with (111) at 22.5^{o} , (171) at 30.2^{o} and a

possible $Bi_2Ti_4O_{11}$ phase at 45.3^o respectively. This growth has low crystallinity and also a change in stoichiometry for BIT. Both these losses are highly disadvantageous for device applicatio. The top of the stacked image is an improved version of the growth with a seed layer using STO. Along with the standard silicon peaks, there are perovskite peaks associated with a (100) STO. These peaks occurs at 23.4^o (001) and 46.5^o (002). Orthorhombic BIT has its peaks matched with those of STO. The peaks were determined using a comparison with JCPDS No. 35-0795 [82] for an orthorhombic BIT.

LNB

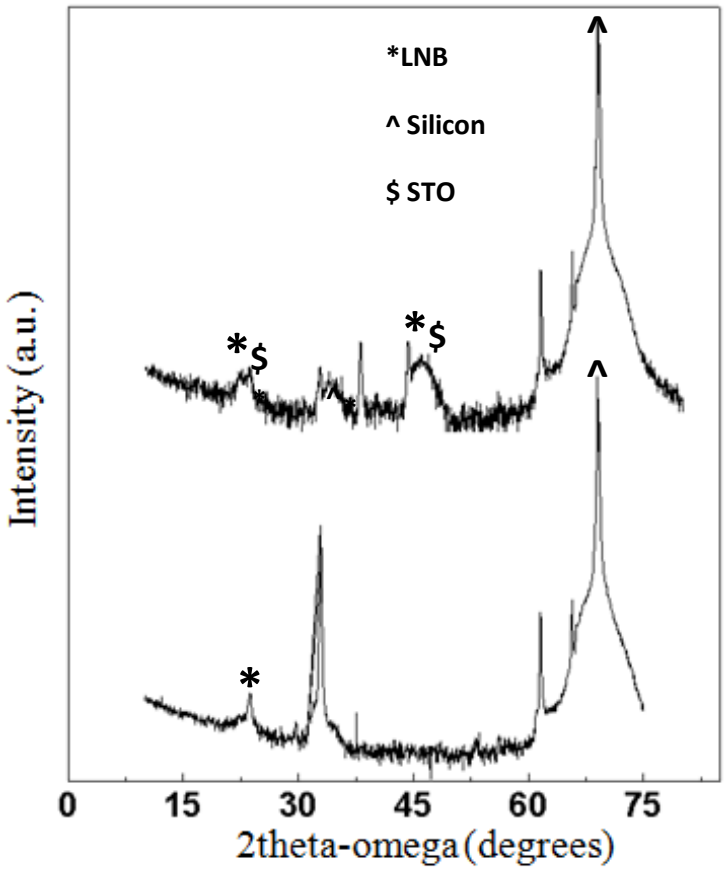

Figure 6.5: Plots for LNB grown on Si (bottom) and STO/Si are shown.

LNB grown on Si (100) substrate produces the standard silicon peaks along with a (012) peak at 23.5^{o} indicating a rhombohedral LNB phase. The top image in the stacked figure 6.5 shows the perovskite peaks of STO along with rhombohedral peaks of LNB at 23.5^{o} (012) and a (006) peak at 39^{o}. JCPDS no. 20-0631 [83] was used to confirm the growths for a rhombohedral LNB.

VII. FUTURE WORK

Growths involving BMO, PZT, LNB and BIT have been successfully demonstrated. More-than-Moore is about diversification and the beginning of diversification starts with successful integration of functional materials onto silicon substrates. We have demonstrated successful growths using two unique growth approaches, these being MBE and CSD. The versatility of functional oxides to observe a wide range of properties makes them for excellent candidates in novel device applications.

BMO is a multiferroic and has long been pegged as a possible replacement for use in low power memory devices. BMO research has seen tremendous growth using STO substrates and as a bulk material. However its epitaxial integration onto Si had remained elusive. The reasons for the lack of success in growth range from MBE techniques being expensive to that of the difficulty in establishing the right reactive environment for BMO formation. In addition there are also issues concerning lattice mismatch between BMO and Si. Within this thesis we demonstrated that using a virtual substrate, in the form of STO, epitaxial BMO can be grown albeit with great difficulty on Si substrates. The success of growth is the beginning and future work needs to be complimented with electrical and magnetic characterization techniques.

We have also demonstrated a methodology in which crystalline phase of PZT can be optimized to achieve high polarization. This was done using an intentionally grown pyrochlore rich PZT and compared to a perovskite rich PZT by means of ferroelectric hysteresis and XRD patterns. Additional growths were optimized from these preliminary

tests and we were able to obtain a growth that's twice in performance compared to a non-optimized growth. We have also put forward ideas involving higher increase in performance by tuning annealing, intermediate bake and cooling rate temperatures. Growths were also performed on Si substrates with no virtual substrates/seeding layers and it's been concluded that for increased crystallinity, in perovskite phase pure PZT, a seeding layer is vital.

Optically active materials such as LNB don't yet find applications in full fledged oxide based devices such as FERROFETs. They have been either used as stand-alone materials or incorporated directly onto silicon for purely optical purposes such as waveguides etc. Hence research has been sparse to absent in these types of applications. Successful growth of LNB on STO buffered Si substrates has been established within this thesis. Further characterization is necessary before ideas for novel applications are brought forth.

BIT is yet another material with great potential for use in oxide based devices. It is a leading prospect among lead-free ferroelectrics to replace PZT for uses in sensors, actuators and memory devices. Similar to PZT, BIT is extremely stoichiometry sensitive and therefore poses challenges for growth. As much as the thesis established a successful of BIT, there is plenty of room for environment.

This is the same case with all the growths within the thesis. As discussed in chapter II, symmetry breaking is fundamental to generate materials that are highly functional. Hence care needs to be taken in generating materials that are as close to single crystal as possible.

REFERENCES

1 G. E. Moore, "Cramming more Components onto Integrated Circuit," *Electronics,* vol. 38, no. 8, pp. 114-117, 1965.

2 W. Arden, M. Brillouet, P. Cogez, M. Graef, B. Huizing and R. Mahnkopf, "More-than-Moore," ITRS, Santa Clara, 2010.

3 H. Iwai, "Roadmap for 22nm and beyond," *Microelectronic Engineering,* vol. 86, no. 7-9, pp. 1520-1528, 2009.

4 P. S. Otellini, "Intel : Investor Meeting 2012," Intel, Santa Clara, 2012.

5 A. Brand, "Precision Materials to Meet Scaling Challenges Beyond 14nm," Semicon : Applied Materials, San Francisco, 2013.

6 D. Schlom, C. L.Q., P. X.Q., A. Schmehl and M. Zurbuchen, "A Thin Film Approach to Engineering Functionality into Oxides," *Journal of the American Ceramic Society,* vol. 91, no. 8, pp. 2429-2454, 2008.

7 D. W. Bruce, D. O'Hare and R. I. Walton, Functional Oxides, West Sussex: John Wiley & Sons, 2010.

8 R. Ramesh and N. A. Spaldin, "Multiferroics : Progress and Prospects in Thin Films,"*Nature Materials,* vol. 6, no. 1, pp. 21-29, 2007.

9 N. A. Hill, "Why are there so few magnetic ferroelectrics?," *Journal of Physical Chemistry,* vol. 104, no. 29, pp. 6694-6709, 2000.

10 S. Dong and J. M. Liu, "Recent progress of multiferroic perovskite manganites," *Modern Physics Letters B,* vol. 26, no. 9, p. 12300004(25 pages), 2012.

11 J.F.Scott and C.A. Paz de Araujo, "Ferroelectric Memories," *Science,* Vol. 246, No.4936 , pp. 1400-1405, 1989.

12 A.I.Khan, D. Bhowmik, P.Yu, S.J.Kim , X.Pan, R.Ramesh and S. Salahuddin,"Experimental Evidence of Ferroelectric Negative Capacitance in Nanoscale Heterostructures," *Applied Physics Letters,* Vol. 99, pp. 113501-113504, 2011.

13 S. Vitkavag, "3D Integration : Why, What, Who, When ?," 2007. [Online]. Available: http://www.future-fab.com/documents.asp?d_ID=4396.. [Accessed 2013].

14 H. Schmid, "Multi-ferroic magnetoelectrics," *Ferroelectrics,* vol. 1, no. 162, pp. 317-338, 1994.

15 M. Fiebig, "Revival of magnetoelectric effect," *J.Phys. D: Appl. Phys,* no. 38, pp. 123-152, 2005.

16 P. Curie, "Sur la symétrie dans les phénomènes physiques. Symétrie d'un champ électrique d'un champ magnétique," *J Phys.,* vol. 3, pp. 393-416, 1894.

17 J. Valasek, "Piezoelectric and allied phenomena in Rochelle salt," *Phys. Rev.,* vol. 15, pp. 475-481, 1920.

18 H. Heesch, "Zur Struckturtheorie der ebenen symmetrigruppen," *Z. Kristallogr.,* no. 71, pp. 95-102, 1929.

19 A. V. Shubnikov, "Symmetry and Antisymmetry of Finite Figures," *USSR Academy of Sciences,* p. 172, 1951.

20 L. A. Shuvalov and N. V. Belov, "The symmetry of crystals in which ferromagnetic and ferroelectric properties appear simultaneously," *Kristallografiaya*, vol. 7, pp. 192-197, 1962.
21 L. D. Landau, "On the theory of phase transitions," *Eksp. Teor. Fiz.*, vol. 7, pp. 19-32, 1937.
22 L. D. Landau and E. M. Lifshitz, Electrodynamics of Continuous Media, Moscow: Gostekhizdat, 1957.
23 D. N. Astrov, "Magnetoelectric effect in chromium oxide," *Sov. Phys. JETP*, no. 13, pp. 729-733, 1961.
24 I. E. Dzyaloshinskii, "On the magneto-electrical effect in antiferromagnets," *Sov. Phys. JETP*, no. 10, p. 628, 1959.
25 G. A. Smolensky and V. A. Ioffe, "Communication No. 71," in *Colloque International du Magnetisme*, Grenoble, 1958.
26 E. Ascher, H. Rieder, H. Schmid and H. Stossel, "Some properties of ferromagnetoelectric nickel-iodine Boracite, Ni(3)B(7)O(13)I," *J. Appl. Phys.*, no. 37, pp. 1404-1405, 1966.
27 J. F. Nye, Physical Properties of Crystals: Their Representation by Tensors and Matrices, Oxford University Press, 1985.
28 S. Halasyamani, "Superferroelectrics & non-linear optical (NLO) materials," UCSB - Chemical Bonding Center, [Online]. Available: http://www.cdm.ucsb.edu/pages/research1.html. [Accessed November 2013].
29 C. Yoder, Ionic Compounds: Applications of Chemistry to Mineralogy, Wiley, 2006.
30 J. Casson, K. Gahagan, D. Scrymgeour, R. Jain, J. Robinson, V. Gopalan and R. Sander, "Electro-optic coefficients of lithium tantalate," *J. Opt. Soc. Am.*, vol. 21, no. 11, pp. 1948-1952, 2004.
31 A. Garcia and D. Venderbilt, "Electromechanical behavior of BaTiO3 from first principles," *Applied Physics Letters*, vol. 72, no. 23, pp. 2981-2983, 1998.
32 E. Hartmann, "Introduction to Crystal Physics," International Union of Crystallography - University College Cardiff Press, Cardiff, 2001.
33 P. Chandra and P. B. Littlewood, "A Landau Primer for Ferroelectrics," *Physics of Ferroelectrics*, vol. 105, pp. 69-116, 2007.
34 M. Dawber, "Research," Stony Brook Univ., 21 05 2013. [Online]. Available: http://mini.physics.sunysb.edu/~mdawber/research.htm. [Accessed 11 2013].
35 W. Erenstein, N. D. Mathur and J. F. Scott, "Multiferroic and magnetoelectric materials," *Nature*, vol. 442, no. 17, pp. 759-765, 2006.
36 Schlom. et.al, "Room temperature ferroelectricity in strained SrTiO3," *Nature*, vol. 430, pp. 758-761, 2004.
37 N. Spaldin, Magnetic Materials : Fundamentals and Device Applications, Cambridge University Press, 2003.
38 H. Schmid, "Some symmetry aspects of ferroics and single phase multiferroics," *J. Phys.: Condens. Matter*, vol. 20, p. 434201 (24), 2008.
39 N. A. Hill and K. M. Rabe, "First-Principles Investigation of Ferromagnetism and Ferroelectricity in Bismuth Manganite," *Physical Review B*, vol. 59, no. 13, pp. 8759-8769, 1999.

40 R. Seshadri and N. H. Hill, "Visualizing the Role of Bi 6s "Lone Pairs" in the Off-Center Distortion in Ferromagnetis BiMnO3," *Chem. Mater.,* vol. 13, no. 9, pp. 2892-2899, 2001.

41 A. F. Moreira dos Santos, A. K. Cheetham, W. Tian, X. Pan, Y. Jia, N. J. Murphy, J. Lettieri and D. G. Schlom, "Epitaxial Growth and Properties of Metastable BiMnO3 Thin Films," *Applied Physics Letters,* vol. 84, no. 1, pp. 91-93, 2004.

42 J. H. Lee, X. Ke, R. Misra, J. F. Ihlefeld, X. S. Xu, Z. G. Mei, T. Heeg, M. Roeckerath, J. Schubert, Z. K. Liu, J. L. Musfeldt, P. Schiffer and D. G. Schlom, "Adsorption-Controlled Growth of BiMnO3 Films by Molecular-Beam Epitaxy," *Applied Physics Letters,* vol. 96, pp. 262905-262908, 2010.

43 J. D. Coey, M. Viret and S. V. M. Molnar, "Mixed-Valence Manganites," *Advances in Physics,* vol. 48, no. 2, pp. 167-293, 1999.

44 Y. Zhang, D. Wang, J. Wang, Q. Chen, Z. Zhang, X. Pan, Z. Miao, B. Zhang, Z. Wu and X. Yang, "BiMnO3 Perovskite Catalyst for Slective Catalytic Reduction of NO with NH3 at Low Temperature," *Chinese Journal of Catalysis,* vol. 33, no. 9-10, pp. 1448-1454, 2012.

45 I. Y. Shen, G. Z. Cao, C.-C. Wu and C.-C. Lee, "PZT Thin-Film Meso- and Micro Devices," *Ferroelectrics,* vol. 342, pp. 15-34, 2006.

46 P. Muralt, "Ferroelectric Thin Films for Micro-Sensors and Actuators : A Review," *J. Micromech. Microeng,* vol. 10, pp. 136-146, 2000.

47 G. H. Haertling, "Ferroelectric Ceramics : History and Technology," *J.Am.Ceram.Soc,* vol. 82, no. 4, pp. 797-818, 1999.

48 T. Eisuke, R. Nakamura and I. Hiroshi, "Nonvolatile Memory Operations of Meta-Ferroelectric-Insulator-Semiconductor (MFIS) FETs Using PLZT/STO/Si(100) Structures," *IEEE Electron Device Letters,* vol. 18, no. 4, pp. 160-162, 1997.

49 S. Shigeki and R. Ilangovan, "Metal-Ferroelectric-Insulator-Semiconductor Memory FET with Long Retention and High Endurance," *IEEE Electron Device Letters,* vol. 25, no. 6, pp. 369-371, 2004.

50 T. Hirai, Y. Fujisaki, K. Nagashima, H. Koike and Y. Tarui, "Preparation of SrBi3Ta2O9 Film at Low Temperatures and Fabrication of a Metal/Ferroelectric/Insulator/Semiconductor Field Effect Transistor Using Al/SrBi2Ta2O9/CeO2/Si(100) Structures," *Japanese Journal of Applied Physics,* vol. 36, pp. 5908-5911, 1997.

51 S. Salahuddin and S. Datta, "Can the Subthreshold Swin In a Classical FET be Lowered Below 60 mV/Decade," in *IEDM 2008 : Electron Devices Meeting,* San Francisco, 2008.

52 S. Salahuddin and S. Datta, "Use of Negative Capacitance of Provide Voltage Amplification for Low Power Nanoscale Devices," *Nano Letters,* vol. 8, no. 2, pp. 405-410, 2008.

53 B. Jaffe, R. S. Roth and S. Marzullo, "Properties of Piezoelectric Ceramics in the Solid-Solution Series Lead Titanate-Lead Zirconate-Lead Oxides : Tin Oxide and Lead Titanate-Lead Hafnate," *Journal of Research of the National Beureau of Standards,* vol. 55, no. 5, pp. 239-254, 1955.

54 K. D. Budd, S. K. Dey and D. A. Payne, "Sol-Gel Processing of PbTiO3, PZt and PLZT Thin-Films," *British Ceramic Society Proc.*, vol. 36, pp. 107-121, 1985.

55 R. J. Ong and D. A. Payne, "Processing Effects for Integrated PZT : Residual Stress, Thickness, and Dielectric Properties," *J. Am. Ceram. Soc.*, vol. 88, no. 10, pp. 2839-2847, 2005.

56 N. Izyumskaya, Y. I. Alivov, S. J. Cho, H. Morkoc, H. Lee and Y. S. Kang, "Processing, Structure, Properties, and Applications of PZT Thin Films," *Critical Reviews in Solid State and Materials Sciences,* vol. 32, no. 3, pp. 111-202, 2007.

57 V. A. Isupov, "Comments on the paper "X-ray Study Of the PZT Solid Solutions Near the Morphotropic Phase Transition"," *Solid State Communications,* vol. 17, no. 11, pp. 1331-1333, 1975.

58 J. S. Wright and L. F. Francis, "Phase Development in Si Modified Sol-Gel-Derived Lead Titanate," *J. Mater. Res.*, vol. 8, no. 7, pp. 1712-1720, 1993.

59 G. L. Brennecka, C. M. Parish, B. A. Tuttle, L. N. Brewer and M. A. Rodriguez, "Reversibility of the Perovskite-to-Fluorite Phase Transformation in Lead-Based Thin and Ultrathin Films," *Advance Materials,* vol. 20, pp. 1407-1411, 2008.

60 H. T. Lee, W. I. Lee, Y. H. Kim and C. M. Whang, "The Seeding Effects on the Phase Transformation of Sol-Gel-Derived PZT Powder," *Bull. Korean Chem. Soc.*, vol. 23, no. 8, pp. 1078-1084, 2002.

61 S.-Y. Chen, "Texture Development, Microstructure Evolution, and Crystallization of Chemically Derived PZT Thin Films," *J. Am. Ceram. Soc.,* vol. 81, no. 1, pp. 97-105, 1998.

62 H. Thurnauer and J. Deaderick, "Insulating Material". USA Patent US2429588 A, 2 Oct 1941.

63 I. Coondoo, N. Panwar and A. Kholkin, "Lead-Free Piezoelectrics : Current Status and Perspectives," *Journal of Advanced Dielectrics,* vol. 3, no. 2, p. 1330002(22 pages), 2013.

64 E. Aksel and J. L. Jones, "Advances in Lead-Free Piezoelectric Materials for Sensors and Actuators," *Sensors,* vol. 10, pp. 1935-1954, 2010.

65 T. Jardiel, A. C. Caballero and M. Villegas, "Aurivillius Ceramics : Bi4Ti3O12-Based Piezoelectrics," *Journal of the Ceramics Society of Japan,* vol. 116, no. 4, pp. 511-518, 2008.

66 R. Blinc and J. F. Scott, "Multiferroic Magnetoelectric Fluorides : Why are there so many Magnetic Ferroelectrics ?," *Journal of Physics : Condensed Matter,* vol. 23, no. 11, p. 113202, 2011.

67 R. S. Weis and T. K. Gaylord, "Lithium Niobate : Summary of Physical Properties and Crystal Structure," *Appl. Phys. A,* vol. 37, pp. 191-203, 1985.

68 H. E. Junhui and Y. E. Zhizhen, "Highly C-axis Oriented LiNbO3 Thin Film on Amorphous SiO2 Buffer Layer and Its Growth Mechanism," *Chinese Science Bulletin,* vol. 48, no. 21, pp. 2290-2294, 2003.

69 L. Arizmendi, "Photonic Applications of Lithium Niobate Crystals," *Phys. Stat. Sol.*, vol. 201, no. 2, pp. 253-283, 2004.

70 G. Rosenman, D. Shur, Y. E. Krasik and A. Dunaevsky, "Electron Emission From Ferroelectrics," *Journal of Applied Physics,* vol. 88, no. 11, pp. 6110-6161, 2000.

71 W. C. Wang, B. J. Rodriguez, A. Gruverman and R. J. Nemanich, "Polarization-Dependent Electron Affinity of LiNbO3 Surfaces," *Applied Physics Letters,* vol. 85, no. 12, pp. 2136-2138, 2004.
72 B. T. Matthias and J. P. Remeika, "Ferroelectricity In The Ilmenite Structure," *Phys. Rev.,* vol. 76\, 1949.
73 S. Hirano and K. Kato, "Formation of LiNbO3 Films by Hydrolysis of Metal Alkoxides," *Journal of Non-Crystalline Solids,* vol. 100, no. 1-3, pp. 538-541, 1988.
74 M. Dawber, K. M. Rabe and J. F. Scott, "Physics of Thin-Film Ferroelectric Oxides," *Reviews of Modern Physics,* vol. 77, pp. 1083-1130, 2005.
75 L. W. Martin, Y. H. Chu and R. Ramesh, "Advances In The Growth and Characterization of Magnetic, Ferroelectric, and Multiferroic Oxide Thin Films," *Materials Science and Engineering R,* vol. 68, pp. 89-133, 2010.
76 L. Nistor, G. Van Tendeloo and S. Amelinckx, "The Paraelectric-Ferroelectric Phase Transition of Bi4Ti3O12 Studied by Electron Microscopy," *Phase Transitions,* vol. 59, pp. 135-153, 1996.
77 E. C. Subbarao, "Ferroelectricity in Bi4Ti3O12 and Its Solid Solutions," *Physical Review,* vol. 122, no. 3, pp. 804-807, 1961.
78 T.-Y. Chiou and D.-H. Kuo, "Pure Bi4Ti3O12 Thin Films With Improved Ferroelectric Properties," *Applied Physics Letters,* vol. 85, p. 3196, 2004.
79 X. Q. Pan, J. C. Jiang, C. D. Theis and D. G. Schlom, "Domain Structure of Epitaxial Bi4Ti3O12 Thin Films Grown on (001) SrTiO3 Substrates," *Applied Physics Letters,* vol. 83, no. 12, p. 2315, 2003.
80 A. Hardy, D. Mondelaers, G. Vanhoyland, M. K. Van Bael, J. Mullens and L. C. Van Poucke, "The Formation of Ferroelectric Bismuth Titanate (Bi4Ti3O12) From an Aqueous Metal-Chelate Gel," *Journal of Sol-Gel Science and Technology,* vol. 26, pp. 1103-1107, 2003.
81 W. Liu, X. Wang, D. Tian, C. Xiao, Z. Wei and S. Chen, "Chemical Reaction and Crystalline Procedure of bismuth Titanate Nanoparticles Derived by Metalorganic Decomposition Technique," *Materials Sciences and Applications,* vol. 1, pp. 91-96, 2010.
82 F. Wang, J. Wang, X. Zhong, B. Li, J. Liu, D. Wu, D. Mo, D. Guo, S. Yuan, K. Zhang and Y. Zhou, "Shape-Controlled Hydrothermal Synthesis of Ferroelectric Bi4Ti3O12 Nanostructures," *CrystEngComm,* vol. 15, p. 1397, 2013.
83 J. Liu, D. Xue and K. Li, "Single-Crystalline Nanoporous Nb2O5 Nanotubes," *Nanoscale Research Letters,* vol. 6, p. 138, 2011.